CERN-EP-2020-132  
14 July 2020

## An investigation of the very rare $K^+ \rightarrow \pi^+ \nu \bar{\nu}$ decay

The NA62 Collaboration

### Abstract

The NA62 experiment reports an investigation of the  $K^+ \rightarrow \pi^+ \nu \bar{\nu}$  mode from a sample of  $K^+$  decays collected in 2017 at the CERN SPS. The experiment has achieved a single event sensitivity of  $(0.389 \pm 0.024) \times 10^{-10}$ , corresponding to 2.2 events assuming the Standard Model branching ratio of  $(8.4 \pm 1.0) \times 10^{-11}$ . Two signal candidates are observed with an expected background of 1.5 events. Combined with the result of a similar analysis conducted by NA62 on a smaller data set recorded in 2016, the collaboration now reports an upper limit of  $1.78 \times 10^{-10}$  for the  $K^+ \rightarrow \pi^+ \nu \bar{\nu}$  branching ratio at 90% CL. This, together with the corresponding 68% CL measurement of  $(0.48_{-0.48}^{+0.72}) \times 10^{-10}$ , are currently the most precise results worldwide, and are able to constrain some New Physics models that predict large enhancements still allowed by previous measurements.

*Accepted for publication in JHEP*

## The NA62 Collaboration\*

### **Université Catholique de Louvain, Louvain-La-Neuve, Belgium**

E. Cortina Gil, A. Kleimenova, E. Minucci<sup>1,2</sup>, S. Padolski<sup>3</sup>, P. Petrov, A. Shaikhiev<sup>4</sup>,  
R. Volpe<sup>5</sup>

### **TRIUMF, Vancouver, British Columbia, Canada**

T. Numao, B. Velghe

### **University of British Columbia, Vancouver, British Columbia, Canada**

D. Bryman<sup>6</sup>, J. Fu<sup>7</sup>

### **Charles University, Prague, Czech Republic**

T. Husek<sup>8</sup>, J. Jerhot<sup>9</sup>, K. Kampf, M. Zamkovsky

### **Institut für Physik and PRISMA Cluster of excellence, Universität Mainz, Mainz, Germany**

R. Aliberti<sup>10</sup>, G. Khoraiuli<sup>11</sup>, J. Kunze, D. Lomidze<sup>12</sup>, R. Marchevski<sup>\*,13</sup>, L. Peruzzo,  
M. Vormstein, R. Wanke

### **Dipartimento di Fisica e Scienze della Terra dell'Università e INFN, Sezione di Ferrara, Ferrara, Italy**

P. Dalpiaz, M. Fiorini, I. Neri, A. Norton, F. Petrucci, H. Wahl

### **INFN, Sezione di Ferrara, Ferrara, Italy**

A. Cotta Ramusino, A. Gianoli

### **Dipartimento di Fisica e Astronomia dell'Università e INFN, Sezione di Firenze, Sesto Fiorentino, Italy**

E. Iacopini, G. Latino, M. Lenti, A. Parenti

### **INFN, Sezione di Firenze, Sesto Fiorentino, Italy**

A. Bizzeti<sup>14</sup>, F. Bucci

### **Laboratori Nazionali di Frascati, Frascati, Italy**

A. Antonelli, G. Georgiev<sup>15</sup>, V. Kozhuharov<sup>15</sup>, G. Lanfranchi, S. Martellotti, M. Moulson,  
T. Spadaro

### **Dipartimento di Fisica "Ettore Pancini" e INFN, Sezione di Napoli, Napoli, Italy**

F. Ambrosino, T. Capussela, M. Corvino<sup>13</sup>, D. Di Filippo, P. Massarotti, M. Mirra,  
M. Napolitano, G. Saracino

### **Dipartimento di Fisica e Geologia dell'Università e INFN, Sezione di Perugia, Perugia, Italy**

G. Anzivino, F. Brizioli, E. Imbergamo, R. Lollini, R. Piandani<sup>16</sup>, C. Santoni

### **INFN, Sezione di Perugia, Perugia, Italy**

M. Barbanera<sup>17</sup>, P. Cenci, B. Checcucci, P. Lubrano, M. Lupi<sup>18</sup>, M. Pepe, M. Piccini

### **Dipartimento di Fisica dell'Università e INFN, Sezione di Pisa, Pisa, Italy**

F. Costantini, L. Di Lella, N. Doble, M. Giorgi, S. Giudici, G. Lamanna, E. Lari, E. Pedreschi,  
M. Sozzi

### **INFN, Sezione di Pisa, Pisa, Italy**

C. Cerri, R. Fantechi, L. Pontisso, F. Spinella

**Scuola Normale Superiore e INFN, Sezione di Pisa, Pisa, Italy**

I. Mannelli

**Dipartimento di Fisica, Sapienza Università di Roma e INFN, Sezione di Roma I, Roma, Italy**

G. D'Agostini, M. Raggi

**INFN, Sezione di Roma I, Roma, Italy**

A. Biagioni, E. Leonardi, A. Lonardo, P. Valente, P. Vicini

**INFN, Sezione di Roma Tor Vergata, Roma, Italy**

R. Ammendola, V. Bonaiuto<sup>19</sup>, A. Fucci, A. Salamon, F. Sargeni<sup>20</sup>

**Dipartimento di Fisica dell'Università e INFN, Sezione di Torino, Torino, Italy**

R. Arcidiacono<sup>21</sup>, B. Bloch-Devaux, M. Boretto<sup>13</sup>, E. Menichetti, E. Migliore, D. Soldi

**INFN, Sezione di Torino, Torino, Italy**

C. Biino, A. Filippi, F. Marchetto

**Instituto de Física, Universidad Autónoma de San Luis Potosí, San Luis Potosí, Mexico**

J. Engelfried, N. Estrada-Tristan<sup>22</sup>

**Horia Hulubei National Institute of Physics for R&D in Physics and Nuclear Engineering, Bucharest-Magurele, Romania**

A. M. Bragadireanu, S. A. Ghinescu, O. E. Hutanu

**Joint Institute for Nuclear Research, Dubna, Russia**

A. Baeva, D. Baigarashev, D. Emelyanov, T. Enik, V. Falaleev, V. Kekelidze, A. Korotkova, L. Litov<sup>15</sup>, D. Madigozhin, M. Misheva<sup>23</sup>, N. Molokanova, S. Movchan, I. Polenkevich, Yu. Potrebenikov, S. Shkarovskiy, A. Zinchenko<sup>†</sup>

**Institute for Nuclear Research of the Russian Academy of Sciences, Moscow, Russia**

S. Fedotov, E. Gushchin, A. Khotyantsev, Y. Kudenko<sup>24</sup>, V. Kurochka, M. Medvedeva, A. Mefodev

**Institute for High Energy Physics - State Research Center of Russian Federation, Protvino, Russia**

S. Kholodenko, V. Kurshetsov, V. Obraztsov, A. Ostankov<sup>†</sup>, V. Semenov<sup>†</sup>, V. Sugonyaev, O. Yushchenko

**Faculty of Mathematics, Physics and Informatics, Comenius University, Bratislava, Slovakia**

L. Bician<sup>13</sup>, T. Blazek, V. Cerny, Z. Kucerova

**CERN, European Organization for Nuclear Research, Geneva, Switzerland**

J. Bernhard, A. Ceccucci, H. Danielsson, N. De Simone<sup>25</sup>, F. Duval, B. Döbrich, L. Federici, E. Gamberini, L. Gatignon, R. Guida, F. Hahn<sup>†</sup>, E. B. Holzer, B. Jenninger, M. Koval<sup>26</sup>, P. Laycock<sup>3</sup>, G. Lehmann Miotto, P. Lichard, A. Mapelli, K. Massri, M. Noy, V. Palladino<sup>27</sup>, M. Perrin-Terrin<sup>28, 29</sup>, J. Pinzino<sup>30, 31</sup>, V. Ryjov, S. Schuchmann<sup>32</sup>, S. Venditti

**University of Birmingham, Birmingham, United Kingdom**

T. Bache, M. B. Brunetti<sup>33</sup>, V. Duk<sup>34</sup>, V. Fascianelli<sup>35</sup>, J. R. Fry, F. Gonnella, E. Goudzovski, L. Iacobuzio, C. Lazzeroni, N. Lurkin<sup>9</sup>, F. Newson, C. Parkinson<sup>9</sup>, A. Romano, A. Sergi, A. Sturgess, J. Swallow

**University of Bristol, Bristol, United Kingdom**

H. Heath, R. Page, S. Trilov

**University of Glasgow, Glasgow, United Kingdom**

B. Angelucci, D. Britton, C. Graham, D. Protopopescu

**University of Lancaster, Lancaster, United Kingdom**

J. Carmignani, J. B. Dainton, R. W. L. Jones, G. Ruggiero\*

**University of Liverpool, Liverpool, United Kingdom**

L. Fulton, D. Hutchcroft, E. Maurice<sup>36</sup>, B. Wrona

**George Mason University, Fairfax, Virginia, USA**

A. Conovaloff, P. Cooper, D. Coward<sup>37</sup>, P. Rubin

---

\*Corresponding authors: G. Ruggiero, R. Marchevski,  
email:giuseppe.ruggiero@cern.ch, radoslav.marchevski@cern.ch

†Deceased

<sup>1</sup>Present address: Laboratori Nazionali di Frascati, I-00044 Frascati, Italy

<sup>2</sup>Also at CERN, European Organization for Nuclear Research, CH-1211 Geneva 23, Switzerland

<sup>3</sup>Present address: Brookhaven National Laboratory, Upton, NY 11973, USA

<sup>4</sup>Also at Institute for Nuclear Research of the Russian Academy of Sciences, 117312 Moscow, Russia

<sup>5</sup>Present address: Faculty of Mathematics, Physics and Informatics, Comenius University, 842 48, Bratislava, Slovakia

<sup>6</sup>Also at TRIUMF, Vancouver, British Columbia, V6T 2A3, Canada

<sup>7</sup>Present address: UCLA Physics and Biology in Medicine, Los Angeles, CA 90095, USA

<sup>8</sup>Present address: IFIC, Universitat de València - CSIC, E-46071 València, Spain

<sup>9</sup>Present address: Université Catholique de Louvain, B-1348 Louvain-La-Neuve, Belgium

<sup>10</sup>Present address: Institut für Kernphysik and Helmholtz Institute Mainz, Universität Mainz, Mainz, D-55099, Germany

<sup>11</sup>Present address: Universität Würzburg, D-97070 Würzburg, Germany

<sup>12</sup>Present address: Universität Hamburg, D-20146 Hamburg, Germany

<sup>13</sup>Present address: CERN, European Organization for Nuclear Research, CH-1211 Geneva 23, Switzerland

<sup>14</sup>Also at Dipartimento di Fisica, Università di Modena e Reggio Emilia, I-41125 Modena, Italy

<sup>15</sup>Also at Faculty of Physics, University of Sofia, BG-1164 Sofia, Bulgaria

<sup>16</sup>Present address: Institut für Experimentelle Teilchenphysik (KIT), D-76131 Karlsruhe, Germany

<sup>17</sup>Present address: INFN, Sezione di Pisa, I-56100 Pisa, Italy

<sup>18</sup>Present address: Institut am Fachbereich Informatik und Mathematik, Goethe Universität, D-60323 Frankfurt am Main, Germany

<sup>19</sup>Also at Department of Industrial Engineering, University of Roma Tor Vergata, I-00173 Roma, Italy

<sup>20</sup>Also at Department of Electronic Engineering, University of Roma Tor Vergata, I-00173 Roma, Italy

<sup>21</sup>Also at Università degli Studi del Piemonte Orientale, I-13100 Vercelli, Italy

<sup>22</sup>Also at Universidad de Guanajuato, Guanajuato, Mexico

<sup>23</sup>Present address: Institute of Nuclear Research and Nuclear Energy of Bulgarian Academy of Science (INRNE-BAS), BG-1784 Sofia, Bulgaria

<sup>24</sup>Also at National Research Nuclear University (MEPhI), 115409 Moscow and Moscow Institute of Physics and Technology, 141701 Moscow region, Moscow, Russia

<sup>25</sup>Present address: DESY, D-15738 Zeuthen, Germany

<sup>26</sup>Present address: Charles University, 116 36 Prague 1, Czech Republic

<sup>27</sup>Present address: Physics Department, Imperial College London, London, SW7 2BW, UK

<sup>28</sup>Present address: Aix Marseille University, CNRS/IN2P3, CPPM, F-13288, Marseille, France

<sup>29</sup>Also at Université Catholique de Louvain, B-1348 Louvain-La-Neuve, Belgium

<sup>30</sup>Present address: Department of Physics, University of Toronto, Toronto, Ontario, M5S 1A7, Canada

<sup>31</sup>Also at INFN, Sezione di Pisa, I-56100 Pisa, Italy

<sup>32</sup>Present address: Institut für Physik and PRISMA Cluster of excellence, Universität Mainz, D-55099 Mainz, Germany

<sup>33</sup>Present address: Department of Physics, University of Warwick, Coventry, CV4 7AL, UK

<sup>34</sup>Present address: INFN, Sezione di Perugia, I-06100 Perugia, Italy

<sup>35</sup>Present address: Dipartimento di Psicologia, Università di Roma La Sapienza, I-00185 Roma, Italy

<sup>36</sup>Present address: Laboratoire Leprince Ringuet, F-91120 Palaiseau, France

<sup>37</sup>Also at SLAC National Accelerator Laboratory, Stanford University, Menlo Park, CA 94025, USA

# Contents

<b>1</b>	<b>Introduction</b>	<b>6</b>
<b>2</b>	<b>Principles of the experiment and analysis method</b>	<b>7</b>
<b>3</b>	<b>Experimental setup and data taking</b>	<b>9</b>
<b>4</b>	<b>Data reconstruction and calibration</b>	<b>11</b>
<b>5</b>	<b>Selection of signal and normalization decays</b>	<b>12</b>
5.1	Downstream charged particle . . . . .	12
5.2	Parent beam particle . . . . .	13
5.3	Kaon decay . . . . .	14
5.4	Kinematic regions . . . . .	15
5.5	Pion identification . . . . .	16
5.6	Signal selection . . . . .	17
5.7	Normalization selection . . . . .	19
<b>6</b>	<b>Single Event Sensitivity determination</b>	<b>19</b>
6.1	Number of $K^+ \rightarrow \pi^+\pi^0$ decays . . . . .	20
6.2	Signal and normalization efficiencies . . . . .	20
6.2.1	Monte Carlo efficiencies . . . . .	20
6.2.2	$K^+ \rightarrow \mu^+\nu$ branching ratio measurement . . . . .	24
6.2.3	Random veto efficiency . . . . .	25
6.3	Trigger efficiency . . . . .	26
6.3.1	PNN L0 trigger efficiency . . . . .	27
6.3.2	PNN L1 trigger efficiency . . . . .	27
6.3.3	Trigger efficiency and <i>SES</i> . . . . .	29
6.4	<i>SES</i> result . . . . .	29
<b>7</b>	<b>Expected background</b>	<b>31</b>
7.1	$K^+$ decay background . . . . .	31
7.1.1	$K^+ \rightarrow \pi^+\pi^0$ decay . . . . .	32
7.1.2	$K^+ \rightarrow \mu^+\nu$ decay . . . . .	35
7.1.3	$K^+ \rightarrow \pi^+\pi^+\pi^-$ decay . . . . .	38
7.1.4	$K^+ \rightarrow \pi^+\pi^-e^+\nu$ decay . . . . .	39
7.1.5	Other $K^+$ decays . . . . .	40
7.2	Upstream background . . . . .	41
7.2.1	Background sources . . . . .	41
7.2.2	Upstream background evaluation . . . . .	44
7.3	Summary . . . . .	46
<b>8</b>	<b>Results</b>	<b>46</b>
<b>9</b>	<b>Conclusions</b>	<b>50</b>

# 1 Introduction

The  $K^+ \rightarrow \pi^+ \nu \bar{\nu}$  decay is a flavour-changing Neutral-Current process that proceeds through electroweak box and penguin diagrams in the Standard Model (SM), allowing an exploration of its flavour structure thanks to unique theoretical cleanliness. A quadratic GIM mechanism and the transition of the top quark to the down quark make this process extremely rare. The SM prediction for the  $K^+ \rightarrow \pi^+ \nu \bar{\nu}$  branching ratio (BR) can be written as [1]:

$$\text{BR}(K^+ \rightarrow \pi^+ \nu \bar{\nu}) = \kappa_+ (1 + \Delta_{\text{EM}}) \left[ \left( \frac{\text{Im}\lambda_t}{\lambda^5} X(x_t) \right)^2 + \left( \frac{\text{Re}\lambda_c}{\lambda} P_c(X) + \frac{\text{Re}\lambda_t}{\lambda^5} X(x_t) \right)^2 \right], \quad (1)$$

where  $\Delta_{EM} = -0.003$  accounts for the electromagnetic radiative corrections;  $x_t = m_t^2/M_W^2$ ;  $\lambda = |V_{us}|$  and  $\lambda_i = V_{is}^* V_{id}$  ( $i = c, t$ ) are combinations of Cabibbo-Kobayashi-Maskawa (CKM) matrix elements;  $X$  and  $P_c(X)$  are the loop functions for the top and charm quark respectively; and

$$\kappa_+ = (5.173 \pm 0.025) \times 10^{-11} \left[ \frac{\lambda}{0.225} \right]^8 \quad (2)$$

parameterizes hadronic matrix elements. It is worth noting that  $\text{BR}(K^+ \rightarrow \pi^+ \nu \bar{\nu})$  depends on the sum of the square of the imaginary part of the top loop, which is CP-violating, and the square of the sum of the charm contribution and the real part of the top loop. Numerically, the branching ratio can be written as an explicit function of the CKM parameters,  $V_{cb}$  and the angle  $\gamma$ , as follows :

$$\text{BR}(K^+ \rightarrow \pi^+ \nu \bar{\nu}) = (8.39 \pm 0.30) \times 10^{-11} \left[ \frac{|V_{cb}|}{40.7 \times 10^{-3}} \right]^{2.8} \left[ \frac{\gamma}{73.2^\circ} \right]^{0.74}, \quad (3)$$

where the numerical uncertainty is due to theoretical uncertainties in the NLO (NNLO) QCD corrections to the top (charm) quark contribution [2, 3] and NLO electroweak corrections [4]. The intrinsic theoretical accuracy is at the level of 3.6%. Uncertainties in the hadronic matrix element largely cancel when it is evaluated from the precisely-measured branching ratio of the  $K^+ \rightarrow \pi^0 e^+ \nu$  decay, including isospin-breaking and non-perturbative effects calculated in detail [4, 5, 6]. Using tree-level elements of the CKM matrix as external inputs [7], averaged over exclusive and inclusive determinations, namely  $|V_{cb}| = (40.7 \pm 1.4) \times 10^{-3}$  and  $\gamma = (73.2_{-7.0}^{+6.3})$  degrees, the SM prediction of the branching ratio is  $(8.4 \pm 1.0) \times 10^{-11}$  [1]. The current precision of the CKM parameters dominates the BR uncertainty.

The  $K^+ \rightarrow \pi^+ \nu \bar{\nu}$  decay is sensitive to currently proposed SM extensions and probes higher mass scales than other rare meson decays. This arises because of the absence of tree-level contributions and the quadratic GIM suppression at loop level in the SM, which together lead to a very small BR. Moreover, the absence of long-distance contributions enables the accurate BR calculation. The largest deviations from SM predictions are expected in models with new sources of flavour violation, where constraints from B physics are weaker [8, 9]. Models with currents of defined chirality produce specific correlation patterns between the branching ratios of  $K^+ \rightarrow \pi^+ \nu \bar{\nu}$  and  $K_L \rightarrow \pi^0 \nu \bar{\nu}$  decay modes, which are constrained by the value of the CP-violating parameter  $\varepsilon_K$  [10, 11]. Present experimental constraints limit the range of variation within supersymmetric models [12, 13, 14]. The  $K^+ \rightarrow \pi^+ \nu \bar{\nu}$  decay is also sensitive to some aspects of lepton flavour non-universality [15] and can constrain leptoquark models [16, 17] that aim to explain the measured CP-violating ratio  $\varepsilon'/\varepsilon$  [7].

The E787 and E949 experiments at the Brookhaven National Laboratory (BNL) studied the  $K^+ \rightarrow \pi^+ \nu \bar{\nu}$  decay using a kaon decay-at-rest technique, reaching an overall single event

sensitivity of about  $0.8 \times 10^{-10}$  and measuring the BR to be  $(17.3_{-10.5}^{+11.5}) \times 10^{-11}$  [18, 19]. The NA62 experiment at the CERN SPS will measure more precisely the BR of the  $K^+ \rightarrow \pi^+ \nu \bar{\nu}$  decay using a decay-in-flight technique and data recorded from 2016 to 2018. The first NA62 result was based on the analysis of the data collected in 2016 and proved the feasibility of the technique to study the  $K^+ \rightarrow \pi^+ \nu \bar{\nu}$  decay [20]. In the following sections, NA62 reports the investigation of the  $K^+ \rightarrow \pi^+ \nu \bar{\nu}$  decay, based on data recorded in 2017, corresponding to about 30% of the total data set collected in 2016–18.

## 2 Principles of the experiment and analysis method

The NA62 experiment is designed to reconstruct charged kaons and their daughter particles, when the kaons decay in flight inside a defined fiducial volume. The  $K^+ \rightarrow \pi^+ \nu \bar{\nu}$  decay presents two main challenges: the extremely low value of the SM signal branching ratio of order  $10^{-10}$  and the open kinematics of the final state, as neutrinos remain undetected. These challenges require both the production of a sufficient number of  $K^+ \rightarrow \pi^+ \nu \bar{\nu}$  decays, as can be achieved by exploiting the high-intensity 75 GeV/c secondary  $K^+$  beam produced by the CERN SPS; and the reduction of the contribution of the dominant  $K^+$  decay modes by at least eleven orders of magnitude to bring the background to a level lower than the signal.

The signature of the  $K^+ \rightarrow \pi^+ \nu \bar{\nu}$  decay is a single  $\pi^+$  and missing energy. The squared missing mass,  $m_{\text{miss}}^2 = (P_K - P_{\pi^+})^2$ , where  $P_K$  and  $P_{\pi^+}$  indicate the 4-momenta of the  $K^+$  and  $\pi^+$ , describes the kinematics of the one-track final state. In particular, the presence of two neutrinos makes the signal broadly distributed over the  $m_{\text{miss}}^2$  range, as illustrated in Figure 1. The dominant  $K^+$  decay modes  $K^+ \rightarrow \mu^+ \nu$ ,  $K^+ \rightarrow \pi^+ \pi^0$  and  $K^+ \rightarrow \pi^+ \pi^{+(0)} \pi^{-(0)}$  have different  $m_{\text{miss}}^2$  distributions; it is therefore possible to define regions, either side of the  $K^+ \rightarrow \pi^+ \pi^0$  peak, qualitatively indicated in Figure 1, where the search for the signal is performed, also called *signal regions*.

The  $K^+ \rightarrow \mu^+ \nu$ ,  $K^+ \rightarrow \pi^+ \pi^0$  and  $K^+ \rightarrow \pi^+ \pi^{+(0)} \pi^{-(0)}$  decays enter the signal regions through radiative and/or resolution tails of the reconstructed  $m_{\text{miss}}^2$ . The signal selection, based on kinematics only, relies on the accurate measurement of the  $m_{\text{miss}}^2$  quantity, i.e. of the  $K^+$  and  $\pi^+$  momenta and directions. In contrast,  $K^+ \rightarrow \pi^0 \ell^+ \nu$  or rarer decays, like  $K^+ \rightarrow \pi^+ \pi^- \ell^+ \nu$ , span over the signal regions because of the presence of undetected neutrinos; however, these background decay modes include a lepton in the final state and exhibit extra activity in the form of photons or charged particles. A particle identification system must therefore separate  $\pi^+$  from  $\mu^+$  and  $e^+$ . Photons and additional charged particles in final state must be vetoed as efficiently as possible.

The above conditions translate into the following experimental requirements:

- the detection of incident  $K^+$  and outgoing  $\pi^+$  signals with 100 ps time resolution to mitigate the impact of the pile-up effect due to the high particle rates;
- a low-mass  $K^+$  and  $\pi^+$  tracking system, which reconstructs precisely the kinematics to suppress  $K^+ \rightarrow \pi^+ \pi^0$  and  $K^+ \rightarrow \mu^+ \nu$  backgrounds by at least three orders of magnitude, while keeping the background from hadronic interactions low;
- a system of calorimeters and a Ring Imaging Cherenkov counter (RICH) to suppress decays with positrons and muons by seven to eight orders of magnitude;
- a set of electromagnetic calorimeters, to detect photons and reduce the number of  $K^+ \rightarrow \pi^+ \pi^0$  decays by eight orders of magnitude; and
- an experimental design which guarantees the geometric acceptance for negatively charged particles in at least two detectors.

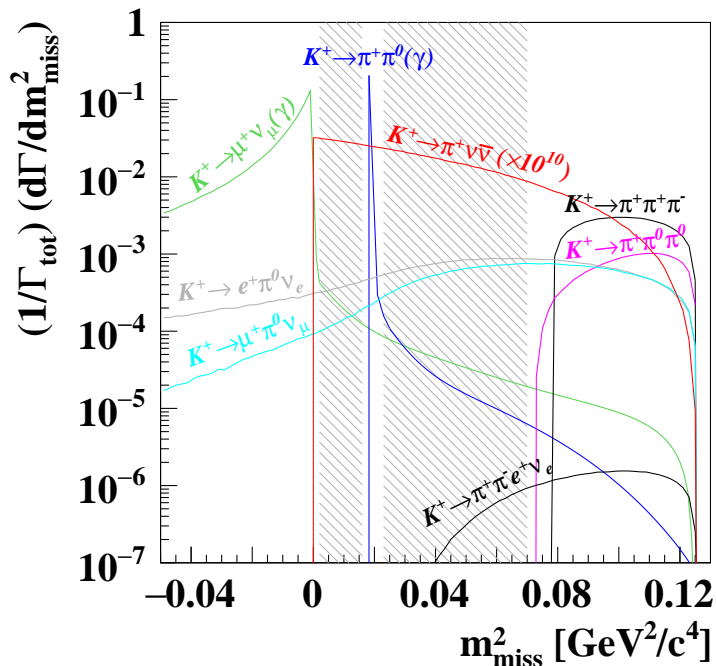


Figure 1: Expected theoretical distributions of the  $m_{\text{miss}}^2$  variable relevant to the  $K^+ \rightarrow \pi^+ \nu \bar{\nu}$  measurement, before applying acceptance and resolution effects. The  $m_{\text{miss}}^2$  is computed under the hypothesis that the charged particle in the final state is a  $\pi^+$ . The  $K^+ \rightarrow \pi^+ \nu \bar{\nu}$  signal (red line) is multiplied by  $10^{10}$  for visibility. The hatched areas include the signal regions.

The decay-in-flight configuration has two main advantages:

- the selection of  $K^+ \rightarrow \pi^+ \nu \bar{\nu}$  decays with a  $\pi^+$  momentum lower than  $35 \text{ GeV}/c$  to facilitate the background rejection by ensuring at least  $40 \text{ GeV}$  of missing energy, and to exploit the capability of the RICH for  $\pi^+/\mu^+$  separation; and
- the achievement of sufficient  $\pi^0$  suppression by using photon detection coverage up to  $50 \text{ mrad}$  with respect to the  $K^+$  direction, and by efficiently detecting photons of energy above  $1 \text{ GeV}$ .

The experimental layout and the data-taking conditions are reviewed in section 3. The reconstruction algorithms are described in section 4. After the  $K^+ \rightarrow \pi^+ \nu \bar{\nu}$  selection (section 5), the analysis proceeds through the evaluation of the single event sensitivity, defined as the branching ratio equivalent to the observation of one SM signal event (section 6). The number of signal decays is normalized to the number of  $K^+ \rightarrow \pi^+ \pi^0$  decays, whose branching ratio is accurately known [7]. This allows the precise determination of the single event sensitivity without relying on the absolute measurement of the total number of  $K^+$  decays. The final step of the analysis is the evaluation of the expected background in the signal regions (section 7). To avoid biasing the selection of  $K^+ \rightarrow \pi^+ \nu \bar{\nu}$  events, the analysis follows a “blind” procedure, with signal regions kept masked until completion of all the analysis steps. Finally, the result is presented in section 8.



### 3 Experimental setup and data taking

The NA62 beam line and detector are sketched in Figure 2. A detailed description of them can be found in [21]. The beam line defines the Z-axis of the experiment's right-handed laboratory coordinate system. The origin is the kaon production target, and beam particles travel in the positive Z-direction. The Y-axis is vertical (positive up), and the X-axis is horizontal (positive left).

The kaon production target is a 40 cm long beryllium rod. A 400 GeV proton beam extracted from the CERN Super Proton Synchrotron (SPS) impinges on the target in spills of three seconds effective duration. Typical intensities during data taking range from  $1.7$  to  $1.9 \times 10^{12}$  protons per pulse (*ppp*). The resulting secondary hadron beam of positively charged particles consists of 70%  $\pi^+$ , 23% protons, and 6%  $K^+$ , with a nominal momentum of 75 GeV/ $c$  (1% rms momentum bite).

Beam particles are characterized by a differential Cherenkov counter (KTAG) and a three-station silicon pixel matrix (Gigatracker, GTK, with pixel size of  $300 \times 300 \mu\text{m}^2$ ). The KTAG uses  $\text{N}_2$  gas at 1.75 bar pressure (contained in a 5 m long vessel) and is read out by photomultiplier tubes grouped in eight sectors. It tags incoming kaons with 70 ps time-resolution. The GTK stations are located before, between, and after two pairs of dipole magnets (a beam achromat), forming a spectrometer that measures beam particle momentum, direction, and time with resolutions of 0.15 GeV/ $c$ , 16  $\mu\text{rad}$ , and 100 ps, respectively.

The last GTK station (GTK3) is immediately preceded by a 1 m thick, variable aperture steel collimator (final collimator). Its inner aperture is typically set at  $66 \text{ mm} \times 33 \text{ mm}$ , and its outer dimensions are about 15 cm. It serves as a partial shield against hadrons produced by upstream  $K^+$  decays.

GTK3 marks the beginning of a 117 m long vacuum tank. The first 80 m of the tank define a volume in which 13% of the kaons decay. The beam has a rectangular transverse profile of  $52 \times 24 \text{ mm}^2$  and a divergence of 0.11 mrad (rms) in each plane at the decay volume entrance.

The time, momentum, and direction of charged daughters of kaon decays-in-flight are measured by a magnetic spectrometer (STRAW), a ring-imaging Cherenkov counter (RICH), and two scintillator hodoscopes (CHOD and NA48-CHOD). The STRAW, consisting of two pairs of straw chambers on either side of a dipole magnet, measures momentum-vectors with a resolution,  $\sigma_p/p$ , between 0.3% and 0.4%. The RICH, filled with neon at atmospheric pressure, tags the decay particles with a timing precision of better than 100 ps and provides particle identification. The CHOD, a matrix of tiles read out by SiPMs, and the NA48-CHOD, comprising two orthogonal planes of scintillating slabs reused from the NA48 experiment, are used for triggering and timing, providing a time measurement with 200 ps resolution.

Other sub-detectors suppress decays into photons or into multiple charged particles (electrons, pions or muons) or provide complementary particle identification. Six stations of plastic scintillator bars (CHANTI) detect, with 1 ns time resolution, extra activity, including inelastic interactions in GTK3. Twelve stations of ring-shaped electromagnetic calorimeters (LAV1 to LAV12), made of lead-glass blocks, surround the vacuum tank and downstream sub-detectors to achieve hermetic acceptance for photons emitted by  $K^+$  decays in the decay volume at polar angles between 10 and 50 mrad. A 27 radiation-length thick, quasi-homogeneous liquid krypton electromagnetic calorimeter (LKr) detects photons from  $K^+$  decays emitted at angles between 1 and 10 mrad. The LKr also complements the RICH for particle identification. Its energy resolution in NA62 conditions is  $\sigma_E/E = 1.4\%$  for energy deposits of 25 GeV. Its spatial and time resolutions are 1 mm and between 0.5 and 1 ns, respectively, depending on the amount and type of energy released. Two hadronic iron/scintillator-strip sampling calorimeters (MUV1,2) and an array of scintillator tiles located behind 80 cm of iron (MUV3) supplement the pion/muon identification system. MUV3 has a time resolution of 400 ps. A lead/scintillator shashlik calorimeter

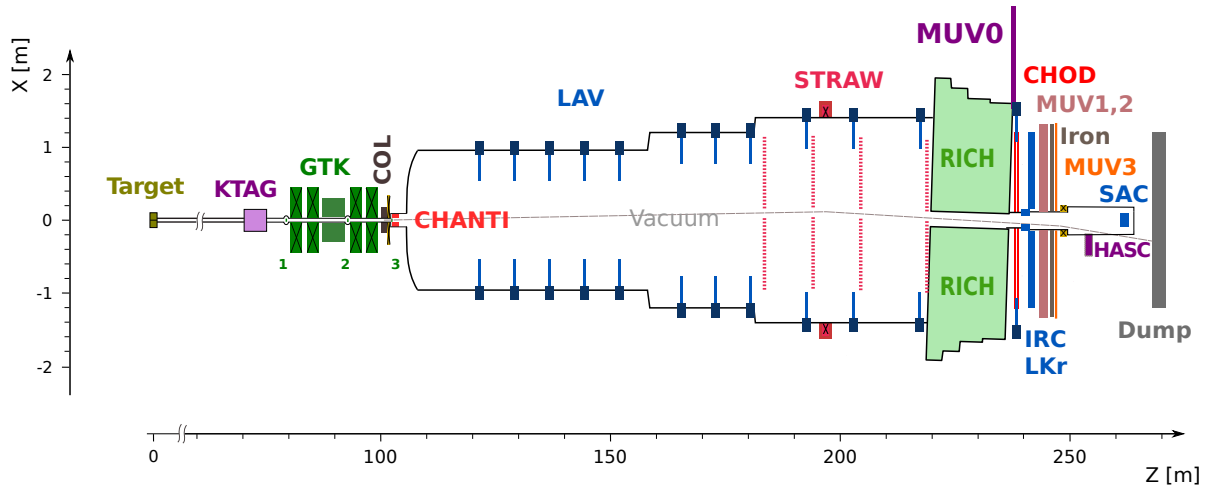


Figure 2: Schematic top view of the NA62 beam line and detector. Dipole magnets are displayed as boxes with superimposed crosses. The label “COL” denotes the collimator named “final collimator” in the text. The label “CHOD” refers both to the CHOD and NA48-CHOD detectors. Also shown is the trajectory of a beam particle in vacuum which crosses all the detector apertures, thus avoiding interactions with material. A dipole magnet between MUV3 and SAC deflects the beam particles out of the SAC acceptance.

(IRC) located in front of the LKr, covering an annular region between 65 and 135 mm from the Z-axis, and a similar detector (SAC) placed on the Z-axis at the downstream end of the apparatus, ensure the detection of photons down to zero degrees in the forward direction. Additional counters (MUV0, HASC) installed at optimized locations provide nearly hermetic coverage for charged particles produced in multi-track kaon decays.

All detectors are read out with TDCs, except for LKr and MUV1, 2, which are read out with 14-bit FADCs. The IRC and SAC are read out with both. All TDCs are mounted on custom-made (TEL62) boards, except for GTK and STRAW, which each have specialized TDC boards. TEL62 boards both read out data and provide trigger information. A dedicated processor interprets calorimeter signals for triggering. A dedicated board (L0TP) combines logical signals (primitives) from the RICH, CHOD, NA48-CHOD, LKr, LAV, and MUV3 into a low-level trigger (L0) whose decision is dispatched to sub-detectors for data readout [22]. A software trigger (L1) exploits reconstruction algorithms similar to those used offline with data from KTAG, LAV, and STRAW to further cull the data before storing it on disk [21].

The data come from  $3 \times 10^5$  SPS spills accumulated during a four-month data-taking period in 2017, recorded at an average beam intensity of 450 MHz. The instantaneous beam intensity is measured event-by-event using the number of signals recorded out-of-time in the GTK detector. The average beam intensity per spill was stable within  $\pm 10\%$  throughout the data-taking period, while the instantaneous beam intensity showed fluctuations up to a factor of two around the average value.

The data have been collected using a trigger specifically setup for the  $K^+ \rightarrow \pi^+ \nu \bar{\nu}$  measurement, called *PNN trigger*, concurrently with a minimum-bias trigger. The PNN trigger is defined as follows. The L0 trigger requires a signal in the RICH to tag a charged particle. The time of this signal, called trigger time, is used as a reference to define a coincidence within 6.3 ns of: a signal in one to four CHOD tiles; no signals in opposite CHOD quadrants to suppress  $K^+ \rightarrow \pi^+ \pi^+ \pi^-$  decays; no signals in MUV3 to reject  $K^+ \rightarrow \mu^+ \nu$  decays; less than 30 GeV

energy deposited in LKr and no more than one cluster to reject  $K^+ \rightarrow \pi^+\pi^0$  decays. The L1 trigger requires: a kaon identified in KTAG; signals within 10 ns of the trigger time in at most two blocks of each LAV station; at least one STRAW track corresponding to a particle with momentum below 50 GeV/ $c$  and forming a vertex with the nominal beam axis upstream of the first STRAW chamber. Events collected by the PNN trigger are referred to as *PNN* events or data. The minimum-bias trigger is based on NA48-CHOD information downscaled by a factor of 400. The trigger time is the time of the NA48-CHOD signal. Data collected by the minimum-bias trigger are used at analysis level to determine the  $K^+$  flux, to measure efficiencies, and to estimate backgrounds. These data are called *minimum-bias* events or data.

Acceptances and backgrounds are evaluated using Monte Carlo (MC) simulation based on the GEANT4 toolkit [23] to describe detector geometry and response. The  $K^+$  decays are generated in the kaon rest frame using the appropriate matrix elements and form factors. The simulation also includes a description of the collimators and dipole and quadrupole magnets in the beam line, necessary to accurately simulate the beam shape. Certain aspects of the simulation are tuned using input from data, namely signal formation and readout detector inefficiencies. Accidental activity is added to the KTAG Cherenkov counter and to the GTK beam tracker assuming 450 MHz beam intensity, and using a library of pileup beam particles built from data. No accidental activity is simulated in the detectors downstream of the last station of the beam tracker. Simulated data are subjected to the same reconstruction and calibration procedures as real data.

## 4 Data reconstruction and calibration

The channels of the Cherenkov beam counter KTAG are time-aligned with the trigger time, and signals are grouped within 2 ns wide windows to define KTAG candidates. A  $K^+$  KTAG candidate must have signals in at least five of eight sectors.

The arrival time of the pulses measured in each of the GTK pixels is aligned to the trigger time and corrected for pulse-amplitude slewing. Signals from the three GTK stations grouped within 10 ns of the trigger time form a beam track. A track must have pulses in all three stations, therefore it is made of at least three hit pixels. Nevertheless, a particle can leave a signal in more than one adjacent pixel in the same station if hitting the edge of a pixel or because of  $\delta$ -rays. In this case, pulses in neighbouring pixels form a cluster that is used to reconstruct the track. Fully reconstructed  $K^+ \rightarrow \pi^+\pi^+\pi^-$  decays in the STRAW spectrometer are used to align the GTK stations transversely to a precision of better than 100  $\mu\text{m}$  and to tune the GTK momentum scale.

The STRAW reconstruction relies on the trigger time as a reference to determine the drift time. A track is defined by space-points in the chambers describing a path compatible with magnetic bending. A Kalman-filter fit provides the track parameters. The  $\chi^2$  fit value and the number of space-points characterize the track quality. Straight tracks collected with the magnet off serve to align the straw tubes to 30  $\mu\text{m}$  accuracy. The average value of the  $K^+$  mass reconstructed for  $K^+ \rightarrow \pi^+\pi^+\pi^-$  decays provides fine tuning of the momentum scale to a part per thousand precision.

Two algorithms reconstruct RICH ring candidates, both grouping signals from photomultipliers (PM) in time around the trigger time. The first one, called *track-seeded ring*, makes use of a STRAW track as a seed to build a RICH ring and compute a likelihood for several mass hypotheses ( $e^+$ ,  $\mu^+$ ,  $\pi^+$  and  $K^+$ ). The second one, called *single ring*, fits the signals to a ring assuming that they are produced by a single particle, with the fit  $\chi^2$  characterizing the quality of this hypothesis. Positrons are used to calibrate the RICH response and align the twenty RICH mirrors to a precision of 30  $\mu\text{rad}$  [24].

The CHOD candidates are defined by the response of two silicon-photomultipliers (SiPM)

reading out the same tile. Signals in crossing horizontal and vertical slabs compatible with the passage of a charged particle form NA48-CHOD candidates. Each slab is time-aligned to the trigger time. Time offsets depending on the intersection position account for the effect of light propagation along a slab.

Groups of LKr cells with deposited energy within 100 mm of a seed form LKr candidates (clusters). A seed is defined by a cell in which an energy of at least 250 MeV is released. Cluster energies, positions, and times are reconstructed taking into account energy calibration, non-linearity, energy sharing for nearby clusters and noisy cells. The final calibration is performed using positrons from  $K^+ \rightarrow \pi^0 e^+ \nu$  decays. An additional reconstruction algorithm is applied to maximise the reconstruction efficiency. This is achieved by defining candidates as sets of cells with at least 40 MeV energy, closer than 100 mm and in time within 40 ns of each other.

The reconstruction of MUV1(2) candidates relies on the track impact point. Signals in fewer than 8 (6) nearby scintillator strips around the track are grouped to form a candidate. The energy of a candidate is defined as the sum of the energies in the strips, calibrated using weighting factors extracted from dedicated simulations and tested on samples of  $\pi^+$  and  $\mu^+$ .

Candidates in MUV3 are defined by time coincidences of the response of the two PMs reading the same tile. The time of a candidate is defined by the later of the two PM signals, to avoid the effect of the time spread due to the early Cherenkov light produced by particles traversing the PM window.

CHANTI candidates are defined by signals clustered in time and belonging either to adjacent parallel bars or to intersecting orthogonal bars.

Two threshold settings discriminate the CHANTI, LAV, IRC and SAC TDC signals [21]. Thus up to four time measurements are associated with each signal, corresponding to the leading and trailing edge times of the high and low thresholds. The relation between the amplitude of the IRC and SAC pulses provided by the FADC readout, and the energy release is calibrated for each channel after baseline subtraction using a sample of  $K^+ \rightarrow \pi^+ \pi^0$  decays.

Signal times measured by GTK, KTAG, CHOD, RICH and LKr are further aligned to the trigger time for each spill, resulting in a better than 10 ps stability through the whole data sample.

## 5 Selection of signal and normalization decays

The selection of both  $K^+ \rightarrow \pi^+ \nu \bar{\nu}$  signal and  $K^+ \rightarrow \pi^+ \pi^0$  normalization decays requires the identification of the downstream charged particle as a  $\pi^+$  and the parent beam particle as a  $K^+$ . Further specific criteria are applied to separate signal and normalization events.

### 5.1 Downstream charged particle

A downstream charged particle is defined as a track reconstructed in the STRAW spectrometer (downstream track) and matching signals in the two hodoscopes CHOD and NA48-CHOD, in the electromagnetic calorimeter LKr, and in the RICH counter.

The downstream track must include space-points reconstructed in all four chambers of the STRAW spectrometer, satisfy suitable quality criteria, and be consistent with a positively charged particle. The extrapolation of this track to any downstream detector defines the expected position of the charged particle's impact point on that detector. These positions must lie within the geometric acceptance of the corresponding downstream detectors and outside the acceptance of the large and small angle calorimeters LAV and IRC. The impact points of the charged particles are used to match the downstream tracks with signals in the hodoscopes and the electromagnetic calorimeter.

Two discriminant variables are built using the difference of time and spatial coordinates between each hodoscope candidate and the track. The NA48-CHOD candidate with the lowest discriminant value and the CHOD candidate closest in space to the particle impact point are matched to the track. The latter candidate must be within  $\pm 5$  ns of the assigned NA48-CHOD candidate. Cuts on maximum allowed values of the discriminant variables are also implemented to avoid fake or accidental signals in the hodoscopes.

A LKr cluster is matched to a charged particle if its distance from the particle impact point is smaller than 100 mm. The energy released by the track in the calorimeter is defined as the energy of the associated cluster. The time of the associated cluster is the time of the most energetic cell of the cluster. A 2 ns time coincidence is required between the cluster and the NA48-CHOD candidate associated with the track.

The association between the track and a single ring of the RICH counter exploits the relationship between the slope of the track and the position of the ring center. A track-seeded ring is also considered for particle identification purposes (section 5.5). Both types of RICH rings must be in time within  $\pm 3$  ns of the NA48-CHOD candidate associated to the track. The time of the downstream charged particle is defined as the time of the associated RICH single ring.

Track-matching with a CHOD, NA48-CHOD, RICH and LKr candidate is mandatory.

## 5.2 Parent beam particle

The parent  $K^+$  of a selected downstream charged particle is defined by: the  $K^+$  candidate in KTAG closest in time and within  $\pm 2$  ns of the downstream particle; a beam track in GTK associated in time with the KTAG candidate and in space with the downstream track in the STRAW.

The association between GTK, KTAG and STRAW candidates relies on a likelihood discriminant built from two variables: the time difference between the KTAG candidate and the beam track ( $\Delta T(\text{KTAG-GTK})$ ); and the closest distance of approach of the beam track to the downstream charged particle (CDA) computed taking into account bending of the particle trajectory in the stray magnetic field in the vacuum tank. The templates of the  $\Delta T(\text{KTAG-GTK})$  and CDA distributions of the parent  $K^+$  are derived from a sample of  $K^+ \rightarrow \pi^+\pi^+\pi^-$  selected on data. In this case, the clean three-pion final state signature tags the  $K^+$  track in the GTK and one of the positively charged pions is chosen to be the downstream charged particle. The resulting distributions are shown in Figure 3, together with the corresponding distributions for events including a random GTK track instead of the  $K^+$  track. In contrast with the parent  $K^+$ , the shape of the CDA distribution in the presence of random beam tracks depends on the size and divergence of the beam, and the emission angle of the  $\pi^+$ . The beam track with the largest discriminant value is, by construction, the parent  $K^+$ ; its momentum and direction must be consistent with the nominal beam properties.

Because of the high particle rate in the beam tracker, several beam particles may overlap with the  $K^+$  within  $\pm 1$  ns; they are referred to as *pileup* (or *accidental*) particles and the corresponding GTK track is called a pileup (or accidental) track. A *wrong association* occurs when a pileup track leads to a likelihood discriminant value larger than that of the actual  $K^+$  track. An *accidental association* occurs when the  $K^+$  track is not reconstructed in the beam tracker and a pileup track is associated to the downstream charged particle. A sharp cut on the minimum allowed value of the likelihood discriminant reduces the probabilities of wrong and accidental association. Events are also rejected if more than 5 pileup tracks are reconstructed or if the likelihood discriminant values of different beam tracks matching the same downstream charged particle are similar. Finally, a cut is applied on a discriminant computed using the time difference between the beam track and the downstream charged particle, instead of  $\Delta T(\text{KTAG-GTK})$ .

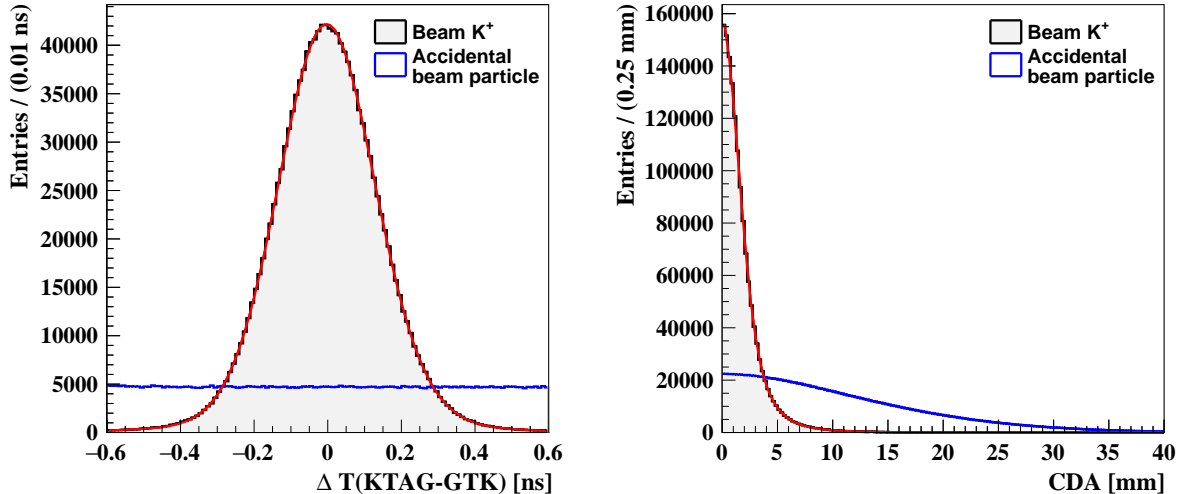


Figure 3: Distributions of  $\Delta T(\text{KTAG-GTK})$  (left) and CDA (right) for events with beam  $K^+$  (shaded histogram) and accidental beam particle (empty histogram), as obtained from fully reconstructed  $K^+ \rightarrow \pi^+\pi^+\pi^-$  decays in the data. The red curves superimposed on the histograms describe the functions used to model the time and CDA distributions of the beam  $K^+$ .

The  $K^+ \rightarrow \pi^+\pi^+\pi^-$  decays allow the performance of the beam-track matching to be monitored. The probabilities of wrong and accidental association depend on the instantaneous beam intensity and are about 1.3% and 3.5% on average, respectively. The latter includes also the probability that a pileup track time is within  $\pm 1$  ns of the KTAG time. Both probabilities depend on the type of process under study.

### 5.3 Kaon decay

A downstream charged particle and its parent  $K^+$  define the kaon decay. The mid-point between the beam and downstream track at the closest distance of approach defines the position of the  $K^+$  decay, called *decay vertex*.

Several downstream charged particles may be reconstructed in the same event as a result of overlapping accidental charged particles in the downstream detectors. In particular, this occurs in the STRAW spectrometer which makes use of a large 200 ns readout window. If two downstream charged particles are reconstructed and both match a parent  $K^+$ , the one closer to the trigger time is accepted. The same trigger time requirement is applied independently to each detector signal matched with beam and downstream tracks. Further conditions are applied to suppress  $K^+$  decay like  $K^+ \rightarrow \pi^+\pi^+\pi^-$ : no more than two tracks reconstructed in the STRAW are allowed in total; if there are two tracks, both must be positively charged and should not form a vertex with a  $Z$ -position between GTK3 and the first STRAW station.

Figure 4 (left) displays the distribution of the longitudinal position ( $Z_{vertex}$ ) of the reconstructed decay vertex of a  $K^+$  decay. The events with  $Z_{vertex} < 100$  m mostly originate from  $K^+$  decays upstream of the final collimator. The peaking structure starting at about 100 m is due to nuclear interactions of beam particles grazing the edges of the final collimator or passing through the last station of the beam tracker located at 103 m. Charged particles created by decays upstream of the final collimator or by nuclear interactions can reach the detectors

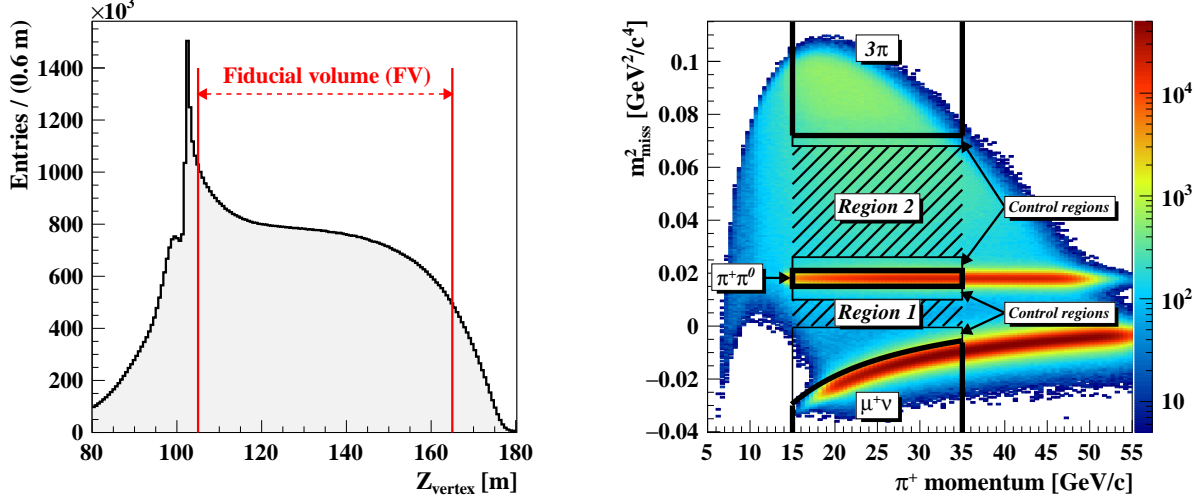


Figure 4: **Left:** distribution of the longitudinal position of the reconstructed decay vertex. The FV is defined between 105 and 165 m (vertical red lines). **Right:** reconstructed  $m_{miss}^2$  as a function of the decay particle momentum for minimum-bias events selected without applying  $\pi^+$  identification and photon rejection, assuming the  $K^+$  and  $\pi^+$  mass for the parent and decay particle, respectively. Signal regions 1 and 2 (hatched areas), as well as  $3\pi$ ,  $\pi^+\pi^0$ , and  $\mu^+\nu$  background regions (solid thick contours) are shown. The control regions are located between the signal and background regions.

downstream and create fake  $K^+$  decays. To mitigate this effect, the decay vertex is required to lie within a fiducial volume (FV) defined as 105 m to 165 m from the target. The coordinates of this vertex must also be consistent with the beam envelope. Wrong or accidental associations or mis-reconstruction of the  $Z_{vertex}$  can shift the origin of these events within the FV, imitating a  $K^+$  decay.

Cuts on the direction of the decay particles as a function of  $Z_{vertex}$  are applied to reduce the number of events reconstructed within the FV, but which actually originated upstream (section 7.2). These cuts are also useful against  $K^+ \rightarrow \pi^+\pi^+\pi^-$  decays with only one  $\pi^+$  reconstructed. The CHANTI detector further protects the FV against nuclear interactions by vetoing events with CHANTI signals within 3 ns of the decay particle candidate. Extra pulses in at least two GTK stations in time with the  $K^+$  candidate may indicate that the  $K^+$  has decayed before entering the decay region. In this case the event is rejected if at least one pileup track is reconstructed in the beam tracker in addition to the  $K^+$  candidate. Finally, events are also discarded if the decay particle track points back to the active area of GTK3.

## 5.4 Kinematic regions

Figure 4 (right) shows the  $m_{miss}^2$  distribution as a function of the decay particle momentum for  $K^+$  decays selected as above from minimum-bias data. Here, the  $m_{miss}^2$  quantity is computed using the three-momenta measured by the beam tracker and the STRAW spectrometer, assuming  $K^+$  and  $\pi^+$  masses. Events from  $K^+ \rightarrow \pi^+\pi^0$  and  $K^+ \rightarrow \mu^+\nu$  decays accumulate at  $m_{miss}^2 = m_{\pi^0}^2$  and  $m_{miss}^2 < 0$ , respectively. Events above  $m_{miss}^2 = 4m_{\pi^+}^2 + (4m_{\pi^0}^2)$  are mostly  $K^+ \rightarrow \pi^+\pi^+\pi^-$  ( $\pi^+\pi^0\pi^0$ ) decays. The shape of the region at low momentum arises from the

$Z_{vertex}$  cuts.

The  $m_{\text{miss}}^2$  resolution varies with  $m_{\text{miss}}^2$  and is about  $10^{-3} \text{ GeV}^2/c^4$  at the  $K^+ \rightarrow \pi^+\pi^0$  peak. This sets the definition of the boundaries of signal region 1 and 2:

**Region 1:**  $0 < m_{\text{miss}}^2 < 0.01 \text{ GeV}^2/c^4$ ;

**Region 2:**  $0.026 < m_{\text{miss}}^2 < 0.068 \text{ GeV}^2/c^4$ .

Additional momentum-dependent constraints supplement this definition by selecting  $m_{\text{miss}}^2$  values computed using either the decay particle momentum measured by the RICH under the  $\pi^+$  mass hypothesis instead of the STRAW momentum, or the nominal beam momentum and direction instead of those measured by the GTK tracker. These requirements are intended to reduce the probability of wrong reconstruction of the  $m_{\text{miss}}^2$  quantity due to a mis-measurement of the momenta of the decay particle or  $K^+$  candidate.

The momentum of the decay particle in the range  $15 - 35 \text{ GeV}/c$  complements the definition of the signal regions. The  $\pi^+$  Cherenkov threshold of the RICH sets the lower boundary at  $15 \text{ GeV}/c$ . The  $K^+ \rightarrow \mu^+\nu$  kinematics and the requirement of a large missing energy drive the choice of the  $35 \text{ GeV}/c$  upper boundary. The two signal regions are kept masked (blind) until the completion of the analysis.

In addition to the signal regions, three exclusive *background regions* are defined:

**The  $\mu\nu$  region:**  $-0.05 < m_{\text{miss}}^2 < m_{\mu\text{-kin}}^2 + 3\sigma$ , where  $m_{\mu\text{-kin}}^2$  is the  $m_{\text{miss}}^2$  of the  $K^+ \rightarrow \mu^+\nu$  decays under the  $\pi^+$  mass hypothesis and  $\sigma$  its resolution;

**The  $\pi^+\pi^0$  region:**  $0.015 < m_{\text{miss}}^2 < 0.021 \text{ GeV}^2/c^4$ ;

**The  $3\pi$  region:**  $0.072 < m_{\text{miss}}^2 < 0.150 \text{ GeV}^2/c^4$ .

Once photons, muons and positrons are rejected (sections 5.5 and 5.6), simulations show that solely  $K^+ \rightarrow \mu^+\nu$ ,  $K^+ \rightarrow \pi^+\pi^0$  and  $K^+ \rightarrow \pi^+\pi^+\pi^-$  decays populate these regions, respectively.

Regions of the  $m_{\text{miss}}^2$  distribution between signal and background regions, referred to as *control regions*, are masked until backgrounds are estimated and then used to validate the estimates. Two regions around the  $\pi^+\pi^0$  peak, for the  $\pi^+\pi^0$  background, and one region each for the  $K^+ \rightarrow \mu^+\nu$  and  $K^+ \rightarrow \pi^+\pi^+\pi^-$  backgrounds, are identified. Both background and control regions are restricted to the  $15 - 35 \text{ GeV}/c$   $\pi^+$  momentum range for consistency with the definition of the signal regions.

## 5.5 Pion identification

The PNN trigger (section 3) discards kaons decaying to muons by vetoing events with a signal in the MUV3 detector. A similar requirement applied offline reinforces the trigger condition, recovering possible online veto inefficiencies and makes the  $\pi^+$  identification in minimum-bias and PNN data identical. Muons may fail to be detected by MUV3 because of inefficiency or catastrophic interaction in the calorimeter, or if they decay upstream.

Pions can be distinguished from muons and positrons using information from the LKr calorimeter and, should any be present, from the MUV1 and MUV2 hadronic calorimeters. A multivariate classifier resulting from a Boosted Decision Tree algorithm, BDT, combines 13 variables characterizing the calorimetric energy depositions. A first group of variables consists of the ratios between the calorimetric energy deposited and the particle momentum measured in the STRAW. The energy in the LKr is used alone, and in combination with the hadronic energies. A second group of variables describes the longitudinal and transverse development of the calorimetric showers. The energy sharing between LKr, MUV1 and MUV2 provides information about the longitudinal shape of the energy deposition, and the shape of the clusters characterizes the transverse size of the shower. Finally, the BDT makes use of the distance between the particle impact point and the reconstructed cluster position. The BDT training is performed using samples of  $\mu^+$ ,  $\pi^+$  and  $e^+$  selected from minimum-bias data recorded in 2016 and not used in the present analysis. The BDT returns the probability for a particle to be a  $\pi^+$ ,



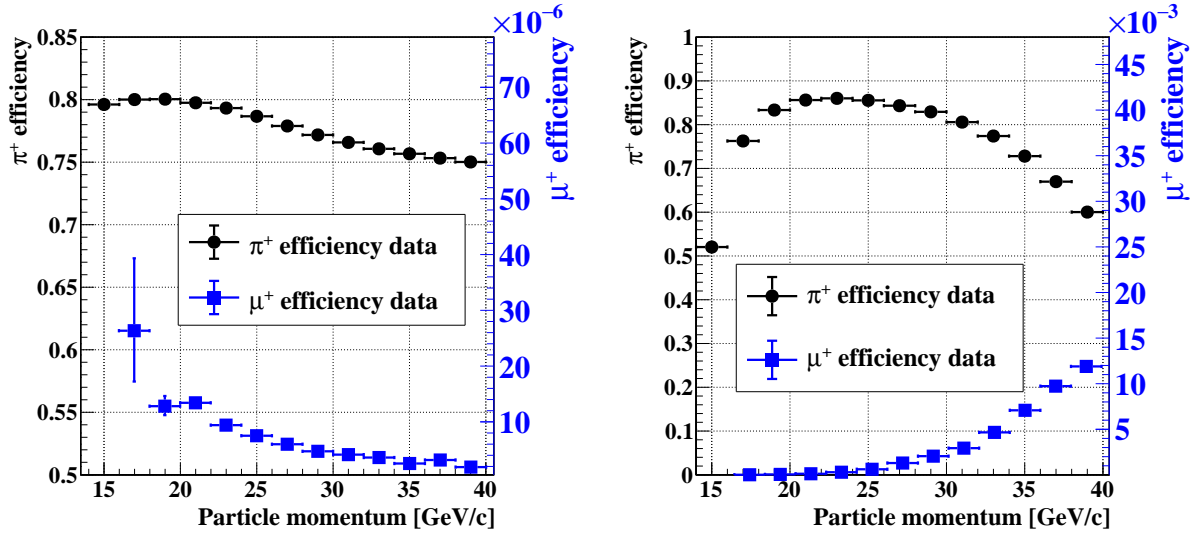


Figure 5: Performance of the  $\pi^+$  identification using calorimeters (left) and RICH (right) measured on data. Performance is quantified in terms of  $\pi^+$  and  $\mu^+$  efficiency, defined as the fraction of pions and muons passing the pion identification criteria, respectively. These criteria include the corresponding RICH and calorimeter reconstruction efficiency. On each plot, the  $\pi^+$  efficiency scale is shown on the left (black) vertical axis, the  $\mu^+$  efficiency (misidentification) scale is shown on the right (blue) vertical axis.

a  $\mu^+$ , or a positron. Pion identification requires the  $\pi^+$  probability to be larger than a minimum value that depends on the particle momentum and is optimised with data.

Samples of  $K^+ \rightarrow \pi^+\pi^0$  and  $K^+ \rightarrow \mu^+\nu$  decays selected from minimum-bias data are used to monitor the performance of the  $\pi^+$  identification efficiency and resulting  $\mu^+$  misidentification probability, shown in Figure 5 (left).

Finally, the RICH separates  $\pi^+$ ,  $\mu^+$  and  $e^+$  independently of the calorimeter responses. The reconstructed mass and the likelihood of the particle must be consistent with the  $\pi^+$  hypothesis. Figure 5 (right) shows the performance of the  $\pi^+/\mu^+$  separation using the RICH as a function of the particle momentum, evaluated using data.

The  $\pi^+$  identification is required for both signal  $K^+ \rightarrow \pi^+\nu\bar{\nu}$  and normalization  $K^+ \rightarrow \pi^+\pi^0$  selections.

## 5.6 Signal selection

Additional requirements are applied to PNN data to reject events with in-time photons or non-accidental additional charged particles in the final state that are compatible with a physics process producing the downstream  $\pi^+$ .

Photon rejection discriminates against partially reconstructed  $K^+ \rightarrow \pi^+\pi^0$  decays. An extra in-time photon in the LKr calorimeter is defined as a cluster located at least 100 mm away from the  $\pi^+$  impact point and within a cluster energy-dependent time coincidence with the  $\pi^+$  time that ranges from  $\pm 5$  ns below 1 GeV to  $\pm 50$  ns above 15 GeV. Pileup clusters can overlap in space with the photon to be rejected, spoiling the time of such a photon by as much as several tens of ns. The choice of a broad timing window at high energy keeps the detection inefficiency below  $10^{-5}$ .

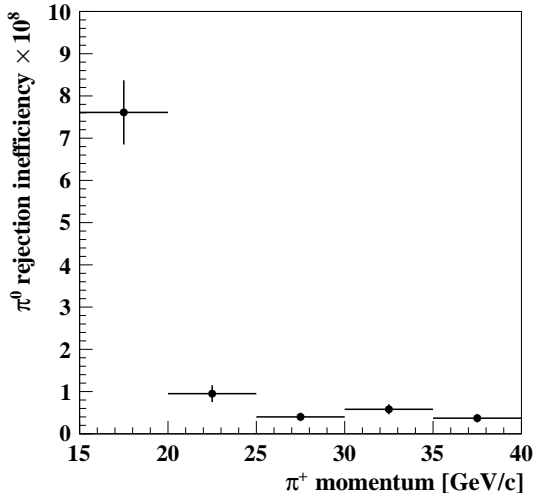


Figure 6: Rejection inefficiency of the  $\pi^0$  from  $K^+ \rightarrow \pi^+\pi^0$  decays as a function of the  $\pi^+$  momentum. The quoted uncertainties are statistical only.

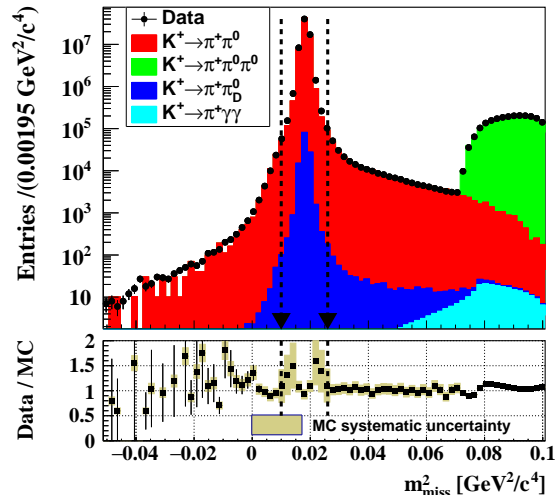


Figure 7: Distribution of the  $m_{\text{miss}}^2$  of events selected from minimum-bias data for normalization. Data and MC simulation are superimposed. The bottom insert shows the data/MC ratio. The error bars correspond to the statistical uncertainty of the ratio, the yellow band is the systematic uncertainty due to the imperfect simulation of the detector response.

An extra in-time photon in the LAV detector is defined as any signal in a LAV station within  $\pm 3$  ns of the  $\pi^+$  time. Appropriate combinations of the TDC leading and trailing edges of the high and low threshold channels define a LAV signal [21]. A similar method identifies photons in the small angle calorimeters IRC and SAC, using a time-window of  $\pm 7$  ns around the  $\pi^+$  time. In addition to the signals from the TDC readout, photon rejection in IRC and SAC exploits the FADC readout; here, a photon signal is defined as an energy deposit larger than 1 GeV in a  $\pm 7$  ns time window.

Multiplicity rejection discriminates against tracks produced by photons interacting in the material before reaching the calorimeters, and against tracks from  $K^+ \rightarrow \pi^+\pi^+\pi^-$  decays partially reconstructed in the STRAW. The first category of charged particles is expected to leave signals in the detectors downstream of the STRAW. The rejection criteria exploit the time and spatial coincidence of isolated signals reconstructed in at least two of the CHOD, NA48-CHOD and LKr detectors. In-time signals in the peripheral detectors MUV0 and HASC are also included. The second category of charged particles is characterized by the presence of track segments, defined as pairs of signals in the first-second or third-fourth STRAW stations and consistent with a particle coming from the FV.

The reduction of reconstructed  $K^+ \rightarrow \pi^+\pi^0$  decays quantifies the performance of the photon and multiplicity rejection. The number of PNN events in the  $\pi^+\pi^0$  region remaining after rejection is compared to the number of minimum-bias events in the same region before rejection. The ratio of these two numbers, corrected for the minimum-bias downscaling factor (section 6) and trigger efficiency (section 6.3), is the rejection inefficiency of the  $\pi^0$  produced in  $K^+ \rightarrow \pi^+\pi^0$

decays. This inefficiency depends on the  $\pi^+$  momentum and is about  $1.3 \times 10^{-8}$  on average, as shown in Figure 6. The measured  $\pi^0$  rejection can be explained in terms of single-photon detection inefficiencies in the LKr, LAV, IRC and SAC calorimeters which are measured from a sample of minimum-bias  $K^+ \rightarrow \pi^+\pi^0$  data using a tag-and-probe method. The estimated  $\pi^0$  efficiency stems from the measured single-photon detection efficiencies convoluted with simulated  $K^+ \rightarrow \pi^+\pi^0$  decays and is in agreement with the measured  $\pi^0$  efficiency within the statistical uncertainty. The rise at low  $\pi^+$  momentum is a consequence of lower detection efficiency for photons travelling close to the beam axis and interacting with the beam pipe.

In addition to the photon and multiplicity rejection, the  $K^+ \rightarrow \pi^+\nu\bar{\nu}$  selection enforces specific requirements against particles entering the FV from upstream. The  $\pi^+$  track is extrapolated back to the  $Z$ -position of the final collimator and the  $X, Y$  transverse coordinates are required to be outside of a box with  $|X| < 100$  mm and  $|Y| < 500$  mm. This cut removes a region with weaker shielding against particles coming from upstream and corresponds to the central aperture of the last dipole magnet of the beam line (section 7.2). This condition is referred to as the *box cut* in the following sections.

Finally, signal selection requires the  $m_{\text{miss}}^2$  value to be within the signal regions defined in section 5.4. The set of criteria described in this section is called *PNN selection* in the following.

## 5.7 Normalization selection

The  $K^+ \rightarrow \pi^+\pi^0$  decays used for normalization are selected from minimum-bias data, as defined in sections 5.3 and 5.5, and their  $m_{\text{miss}}^2$  value must be in the 0.01–0.026 GeV<sup>2</sup>/c<sup>4</sup> range. Figure 7 shows the  $m_{\text{miss}}^2$  spectrum of these events before the  $m_{\text{miss}}^2$  cut, together with the simulated distribution. The shape of the  $K^+ \rightarrow \pi^+\pi^0$  peak depends on the resolution of the STRAW spectrometer, on multiple scattering in the tracker material, on the rate of pileup tracks, and on the calibration of the beam and STRAW trackers. The uncertainty in the simulation of these effects affects the data/MC agreement in the peak region only, and is taken into account in the evaluation of the *SES* (section 6). The overall background under the peak is at the one part per thousand level and stems from  $K^+ \rightarrow \pi^+\pi^0$  decays with  $\pi^0 \rightarrow e^+e^-\gamma$ .

## 6 Single Event Sensitivity determination

Denoting  $N_{K^+}$  the number of kaon decays occurring in the FV, the single-event sensitivity (*SES*) of the present data sample to  $K^+ \rightarrow \pi^+\nu\bar{\nu}$  can be written as

$$SES = \frac{1}{N_{K^+} \cdot \epsilon_{\pi\nu\nu} \cdot \epsilon_{trig}^{PNN}} = \frac{\text{BR}(K^+ \rightarrow \pi^+\pi^0)}{D \cdot N_{\pi\pi}} \frac{\epsilon_{\pi\pi} \cdot \epsilon_{trig}^{MB}}{\epsilon_{\pi\nu\nu} \cdot \epsilon_{trig}^{PNN}}. \quad (4)$$

Here  $N_{\pi\pi}$  is the number of  $K^+ \rightarrow \pi^+\pi^0$  events reconstructed in the FV from minimum-bias data (section 5.7), also called normalization events;  $D$  is the reduction, or down-scaling, factor applied online to reduce the minimum-bias contribution to the total trigger rate;  $\epsilon_{\pi\nu\nu}$  and  $\epsilon_{\pi\pi}$  are the efficiencies to identify a  $K^+ \rightarrow \pi^+\nu\bar{\nu}$  and a  $K^+ \rightarrow \pi^+\pi^0$  decay in the FV, also called signal and normalization efficiencies, respectively;  $\epsilon_{trig}^{PNN}$  and  $\epsilon_{trig}^{MB}$  are the trigger efficiencies that account for the data loss after the event selection due to the PNN and minimum-bias triggers. The efficiencies and  $N_{\pi\pi}$  depend on the  $\pi^+$  momentum,  $p_\pi$ , and on the instantaneous beam intensity,  $I$ . The *SES* is consequently computed in bins of  $p_\pi$  and  $I$ : the momentum range 15–35 GeV/c is subdivided into four bins of 5 GeV/c width and the instantaneous beam intensity into five bins of approximately the same statistics of  $K^+ \rightarrow \pi^+\pi^0$  normalization events.

## 6.1 Number of $K^+ \rightarrow \pi^+\pi^0$ decays

The number of events satisfying the conditions described in section 5.7 is  $N_{\pi\pi} = 68 \times 10^6$ .

The  $\pi^0$  mainly decays to  $\gamma\gamma$ , but in about 1% of cases it decays to  $\gamma e^+ e^-$ , called a Dalitz decay ( $\pi_D^0$ ). The relative impact of  $\pi_D^0$  decays on the *SES* is estimated to be less than 0.3% and is assigned as systematic uncertainty. In the following sections  $K^+ \rightarrow \pi^+\pi^0$  refers only to  $\pi^0 \rightarrow \gamma\gamma$  decays.

## 6.2 Signal and normalization efficiencies

The efficiencies  $\epsilon_{\pi\nu\nu}$  and  $\epsilon_{\pi\pi}$  quantify the effects of reconstruction and selection (section 5) on the counting of signal and normalization channels. Event losses can be grouped into 6 classes:

1. geometric and kinematic acceptances;
2. reconstruction of the  $K^+$  and of the downstream charged particle;
3. matching the  $K^+$  with the downstream charged particle;
4.  $\pi^+$  identification by the RICH and calorimeters;
5. decay region definition; and
6. selection criteria unique to the  $K^+ \rightarrow \pi^+\nu\bar{\nu}$  mode.

The impact of these effects on  $\epsilon_{\pi\nu\nu}$  and  $\epsilon_{\pi\pi}$  depends on the kinematics of the decay, detector resolutions and efficiencies, and the accidental presence of unassociated particles in an event.

The kinematics of the decays are studied with simulations, while detector performance is studied with data and either reproduced by simulation or factored out from  $\epsilon_{\pi\nu\nu}$  and  $\epsilon_{\pi\pi}$ .

Accidental particles have a twofold effect. They affect detector response and therefore the reconstruction of  $K^+$  decays and kinematic resolution. They also randomly satisfy conditions in the GTK, CHANTI, STRAW, MUV3, calorimeters, CHOD, and NA48-CHOD that lead to an event being rejected, referred to here as a random veto. The first effect is modelled with simulation. The second effect, which is independent of decay mode topology, is measured directly with data as a function of the instantaneous beam intensity and factored out of  $\epsilon_{\pi\nu\nu}$  and  $\epsilon_{\pi\pi}$ .

As a consequence, signal and normalization efficiencies may take the form:

$$\epsilon_{\pi\nu\nu} = \epsilon_{\pi\nu\nu}^{MC} \cdot \epsilon_{\pi\nu\nu}^{Random} \quad \epsilon_{\pi\pi} = \epsilon_{\pi\pi}^{MC} \cdot \epsilon_{\pi\pi}^{Random}. \quad (5)$$

The Monte Carlo efficiency,  $\epsilon_{decay}^{MC}$ , quantifies the effects of the factors listed above, except for random losses, and the random efficiency,  $\epsilon_{decay}^{Random}$ , quantifies the fraction of events randomly lost because of the accidental presence of at least one veto condition.

The *SES* depends only on the ratio of the  $\epsilon_{\pi\nu\nu}$  and  $\epsilon_{\pi\pi}$  efficiencies. As both signal and normalization channels contain a  $\pi^+$  in the final state, the ratio effectively cancels significant components of the two efficiencies, decreasing the dependence of the *SES* on their magnitude and reducing significantly their contribution to the *SES* uncertainty.

### 6.2.1 Monte Carlo efficiencies

The Monte Carlo efficiency,  $\epsilon_{decay}^{MC}$ , is the ratio of the number of simulated events passing signal or normalization selection to the corresponding number of generated events in the FV.

Figure 8 shows the values of  $\epsilon_{\pi\pi}^{MC}$  and  $\epsilon_{\pi\nu\nu}^{MC}$  in bins of  $\pi^+$  momentum. The sums over all bins are  $0.087 \pm 0.009$  and  $0.030 \pm 0.003$ , respectively. The uncertainties are systematic, due mainly to the accuracy of  $\pi^+$  identification and  $K/\pi$  track matching in the simulation.

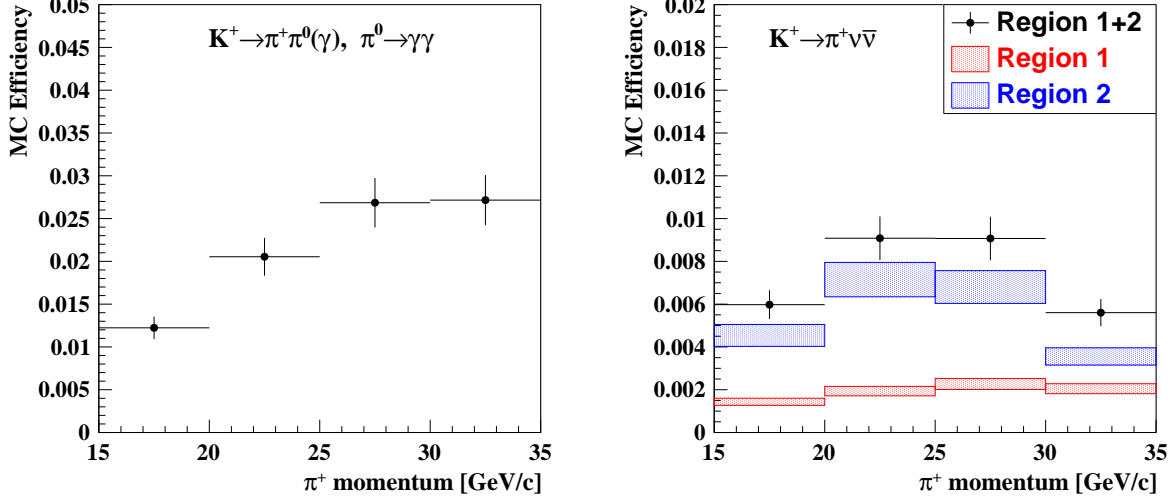


Figure 8: **Left:**  $K^+ \rightarrow \pi^+ \pi^0$  MC efficiency in independent bins of  $\pi^+$  momentum. **Right:**  $K^+ \rightarrow \pi^+ \nu \bar{\nu}$  MC efficiency in independent bins of  $\pi^+$  momentum. The efficiencies in regions 1 and 2 are shown separately and summed (full symbols). The width of the coloured bands represents the uncertainties in the measured values.

Table 1 shows estimates of the contributions to  $\epsilon_{\pi\nu\nu}^{MC}$  and  $\epsilon_{\pi\pi}^{MC}$  of the components listed in section 6.2. The values in the table are approximated, due to correlations among the components. A 10% relative uncertainty is assigned to each component and conservatively considered as 100% correlated. The difference between  $\epsilon_{\pi\nu\nu}^{MC}$  and  $\epsilon_{\pi\pi}^{MC}$  is attributable to differences in acceptance, particle reconstruction, and cuts specific to the signal channel. The accuracy with which these factors are simulated is the primary source of uncertainty in the *SES*. The next paragraphs

Table 1: Monte Carlo efficiencies for normalization and signal decay modes. The uncertainties in the total efficiencies are systematic and reflect the accuracy of the simulation.

Source	$K^+ \rightarrow \pi^+ \pi^0$	$K^+ \rightarrow \pi^+ \nu \bar{\nu}$
Acceptance	0.27	0.16
Particle reconstruction	0.64	0.70
$K^+$ matching	0.84	0.84
$\pi^+$ identification	0.72	0.72
Decay region selection	0.83	0.81
$K^+ \rightarrow \pi^+ \nu \bar{\nu}$ selection	—	0.55
Total	$0.087 \pm 0.009$	$0.030 \pm 0.003$

focus on the contributions from each component of the Monte Carlo efficiencies listed in Table 1.

Table 2: Average detector efficiencies over  $\pi^+$  momentum and instantaneous beam intensity. The uncertainties are estimated by comparing data and simulation, and with systematic studies, such as checks of time stability. The values for the RICH efficiency refer to pion identification efficiencies from  $K^+ \rightarrow \pi^+\nu\bar{\nu}$  and  $K^+ \rightarrow \pi^+\pi^0$ , respectively. All other detector efficiencies are equal for signal and normalization.

Source	Efficiency
KTAG	$0.97 \pm 0.01$
GTK detector	$0.92 \pm 0.02$
GTK reconstruction	$0.94 \pm 0.02$
STRAW	$0.95 \pm 0.01$
RICH	$0.95 \pm 0.03$ ( $0.87 \pm 0.03$ )
CHOD	$> 0.99$
NA48-CHOD	$> 0.99$
LKr	$0.95 \pm 0.03$

### Acceptance

Events fail to be selected because of detector geometry as well as restrictions on the  $\pi^+$  momentum and  $m_{\text{miss}}^2$  ranges. The effects of these three factors are different for signal and normalization selection efficiencies and are therefore a potential source of SES uncertainty.

The impact of the limited accuracy of the simulated  $m_{\text{miss}}^2$  distribution has been quantified by recalculating the *SES* with  $K^+ \rightarrow \pi^+\pi^0$  decays in a smaller  $m_{\text{miss}}^2$  region, (0.015,0.021)  $\text{GeV}^2/c^4$ , where data and MC marginally agree (section 5.7). The corresponding variation of the SES is approximately 1% and assigned as systematic uncertainty due to the simulation of the  $m_{\text{miss}}^2$ .

Detector illumination and the momentum spectrum contribute to a lesser extent to the difference between signal and normalization acceptances. The accuracy of the simulation with respect to these is ascertained by measuring the branching ratio of  $K^+ \rightarrow \mu^+\nu$  normalized to  $K^+ \rightarrow \pi^+\pi^0$ . A systematic uncertainty is assigned after comparing the result of this measurement to the accepted value (section 6.2.2).

### Particle reconstruction

The particle reconstruction efficiency is the product of the KTAG and GTK efficiencies for reconstructing the parent  $K^+$ , and the STRAW, RICH, CHOD, NA48-CHOD and LKr efficiencies for reconstructing the daughter  $\pi^+$ . The RICH, CHOD, NA48-CHOD and LKr efficiencies include detector signal association with a STRAW track.

The effect of local inefficiencies due to detector readout or to accidental activity cancels at first order in the ratio of efficiencies, as signal and normalization decays are recorded simultaneously. Nonetheless, these effects are measured with data and added to the simulation. Table 2 details the impact of the various subdetectors on the reconstruction efficiency. The numbers are averages over  $\pi^+$  momentum between 15 and 35  $\text{GeV}/c$  and instantaneous beam intensity.

KTAG and GTK efficiencies refer to  $K^+$  detection and are equal for signal and normalization. Both efficiencies are measured with data, using  $K^+ \rightarrow \pi^+\pi^+\pi^-$  decays. KTAG inefficiencies come mainly from the readout. GTK inefficiencies arise from geometric acceptance and identified readout malfunctioning (5%) and from the detector (3%) [25]. The GTK reconstruction efficiency is due to the conditions applied to identify a track of good quality.

The efficiency to reconstruct a  $\pi^+$  track with the STRAW is measured with  $K^+ \rightarrow \pi^+\pi^0$  decays in the data. In the 15 – 35 GeV/ $c$  momentum range, the efficiency depends only on the instantaneous beam intensity, which is directly related to accidental activity in the detectors.

The RICH efficiency for reconstructing a  $\pi^+$  with momentum between 15 and 35 GeV/ $c$  is measured with data using  $K^+ \rightarrow \pi^+\pi^0$  decays. It is directly related to the statistics of Cherenkov photons and depends only on the  $\pi^+$  momentum. Simulation reproduces this efficiency with a relative accuracy of about 3%. The simulation indicates that this efficiency is about 7% higher for  $K^+ \rightarrow \pi^+\nu\bar{\nu}$  decays than for  $K^+ \rightarrow \pi^+\pi^0$  decays. This difference is attributable to extra hits created when photons from  $\pi^0$  decay in  $K^+ \rightarrow \pi^+\pi^0$  events convert in RICH material and spoil the charged pion ring shape. Therefore, the RICH reconstruction efficiency does not cancel in the ratio of Equation (4). A sample of  $K^+ \rightarrow \mu^+\nu$  decays in the data is used to test the accuracy of RICH particle reconstruction in the simulation. The resulting ratio of data to MC agrees with that of  $K^+ \rightarrow \pi^+\pi^0$  to within 1.5%. This value is assigned as a relative systematic uncertainty in the *SES* due to the simulation of the RICH reconstruction efficiency.

Measurements with data show that the CHOD and NA48-CHOD detectors are highly efficient. An overall 0.99 efficiency is assigned to account for small losses in the association of detector signals with STRAW tracks that define downstream charged particles.

The LKr calorimeter detects signals from minimum ionizing particles with an efficiency greater than 99%, as measured with data. In the case of  $\pi^+$  inelastic hadronic interactions, an additional inefficiency may arise in associating LKr clusters with STRAW tracks.

### **$K^+$ matching**

The efficiency for matching a  $K^+$  with a downstream charged particle is 0.84 and depends on the GTK efficiency and on time and CDA resolutions. The simulation reproduces the matching performance measured with data to within 5% relative accuracy, once accidental pileup in the GTK and GTK efficiency are simulated. This measurement of the accuracy is taken as a systematic uncertainty in the magnitudes of both  $\epsilon_{\pi\nu\nu}^{MC}$  and  $\epsilon_{\pi\pi}^{MC}$ . However, the effect of  $K^+$  matching is equal for signal and normalization, and therefore no corresponding uncertainty is assigned to the *SES*. As a cross check, the *SES* is found to be nearly insensitive to the simulated level of GTK inefficiency.

### **$\pi^+$ identification**

Not every  $\pi^+$  is identified due to the intrinsic efficiencies of the RICH and calorimeters and to  $\pi^+$  decays in flight.

The RICH efficiency for identifying undecayed  $\pi^+$ s from  $K^+ \rightarrow \pi^+\pi^0$  events is measured with data and found to be about 0.95. Simulation reproduces this number with 3% accuracy and indicates that  $\pi^+$ s from  $K^+ \rightarrow \pi^+\nu\bar{\nu}$  decays are identified with a comparable efficiency.

Simulation reproduces the measured efficiency for the RICH to reconstruct and identify a  $\pi^+$  with an accuracy of about 6%. This value is assigned as a relative uncertainty to  $\epsilon_{\pi\nu\nu}^{MC}$  and  $\epsilon_{\pi\pi}^{MC}$ . However, no additional uncertainty is assigned to the *SES* beyond that from the RICH reconstruction efficiency, because the RICH identification algorithm treats signal and normalization modes the same.

The average efficiency of  $\pi^+$  identification with the calorimeters is about 0.80, as measured with data. Simulation reproduces this result with 2% accuracy. This degree of accuracy is propagated as a relative uncertainty to  $\epsilon_{\pi\nu\nu}^{MC}$  and  $\epsilon_{\pi\pi}^{MC}$ . Simulation also shows that the efficiencies to identify charged pions with the calorimeters are the same for signal and normalization modes. Therefore, the accuracy of calorimeter simulations does not affect the *SES* measurement.

The  $\pi^+$  identification efficiencies reported in Table 1 include an additional factor of 0.95 to account for the probability of  $\pi^+$  decay.

## Decay region

In addition to the definition of the 105–165 m FV, the decay region is shaped by the cuts on the  $\pi^+$  direction as a function of  $Z_{vertex}$  as discussed in section 5.3. These selection criteria reject a slightly different number of signal and normalization events. The simulation accounts for the corresponding effect in the *SES* together with the kinematic and geometric acceptances, as the various contributions are correlated.

## Signal $K^+ \rightarrow \pi^+\nu\bar{\nu}$ selection

Photon and multiplicity rejection and the box cut are applied only to signal events. These selection criteria, therefore, directly impact the measurement of the *SES*.

In the absence of random activity, the box cut alone rejects about 40% of signal events. The GTK, CHANTI, STRAW, and MUV3 veto conditions do not affect  $\epsilon_{\pi\nu\nu}^{MC}$  or  $\epsilon_{\pi\pi}^{MC}$ . On the other hand, because charged pions may interact in RICH material, vetoing photons and extra charged particles can inadvertently reject  $K^+ \rightarrow \pi^+\nu\bar{\nu}$  events. The accuracy with which the simulation models this effect is studied by selecting from data  $K^+ \rightarrow \pi^+\pi^0$  events in which both photons from the  $\pi^0$  decay are detected in LAV stations. The loss of events because of  $\pi^+$  interactions is measured on these data and compared with simulation, leading to about 6% discrepancy. The efficiency  $\epsilon_{\pi\nu\nu}^{MC}$  is corrected for half of this difference. An uncertainty of 100% is assigned to this correction factor, resulting in about 3% relative uncertainty in the *SES*.

## 6.2.2 $K^+ \rightarrow \mu^+\nu$ branching ratio measurement

The measurement of the branching ratio of the  $K^+ \rightarrow \mu^+\nu$  decay provides a test of the accuracy of the MC simulation of the kinematic and geometric acceptances.

The measurement follows a procedure similar to that adopted for the *SES*. The decay  $K^+ \rightarrow \pi^+\pi^0$  is used for normalization and the branching ratio can be expressed as:

$$\text{BR}(K^+ \rightarrow \mu^+\nu) = \text{BR}(K^+ \rightarrow \pi^+\pi^0) \frac{N_{\mu 2}}{\hat{N}_{\pi\pi}} \frac{\hat{\epsilon}_{\pi\pi}}{\epsilon_{\mu 2}}. \quad (6)$$

Here  $N_{\mu 2}$  and  $\hat{N}_{\pi\pi}$  are the number of selected  $K^+ \rightarrow \mu^+\nu$  and  $K^+ \rightarrow \pi^+\pi^0$  events,  $\epsilon_{\mu 2}$  and  $\hat{\epsilon}_{\pi\pi}$  are the efficiencies for selecting them.

Event selection for both modes differs slightly from the procedures described in sections 5.1 and 5.2. Both modes require a RICH ring associated with the STRAW track, but  $\pi^+$  identification for the  $K^+ \rightarrow \pi^+\pi^0$  decay relies on the electromagnetic and hadronic calorimeters only. MUV3 provides positive identification of the  $\mu^+$  from  $K^+ \rightarrow \mu^+\nu$  decay.

The kinematic range  $0.01 < m_{\text{miss}}^2 < 0.026 \text{ GeV}^2/c^4$  defines  $K^+ \rightarrow \pi^+\pi^0$  events. The requirement that  $|m_{\text{miss}}^2(\mu)| < 0.01 \text{ GeV}^2/c^4$  defines  $K^+ \rightarrow \mu^+\nu$  decays. Here,  $m_{\text{miss}}^2(\mu)$  is the squared missing mass computed assuming the particle associated with the STRAW track to be a muon. The background in both selected modes is of the order of  $10^{-3}$ . Estimations of  $\hat{\epsilon}_{\pi\pi}$  and  $\epsilon_{\mu 2}$  rely on Monte Carlo simulations, as for the *SES*. Their magnitudes are about 0.09 and 0.10.

The procedure described in section 6.2 is adopted to quantify the efficiency bias introduced by the simulation of the RICH reconstruction. The corresponding correction factor applied to  $\text{BR}(K^+ \rightarrow \mu^+\nu)$  is  $+0.005 \pm 0.005$ .

The  $\pi^+$  identification efficiency affects only the  $K^+ \rightarrow \pi^+\pi^0$  mode. As stated in section 6.2, this efficiency can be measured with data, and the simulation reproduces the value within 2% accuracy. Half this discrepancy is applied as a correction to  $\hat{\epsilon}_{\pi\pi}$ . Assuming that the uncertainty in this correction is 100%, this amounts to correcting  $\text{BR}(K^+ \rightarrow \mu^+\nu)$  by  $-0.008 \pm 0.008$ .

The  $K^+ \rightarrow \mu^+\nu$  branching ratio is measured to be

$$\text{BR}(K^+ \rightarrow \mu^+\nu) = 0.62 \pm 0.01, \quad (7)$$



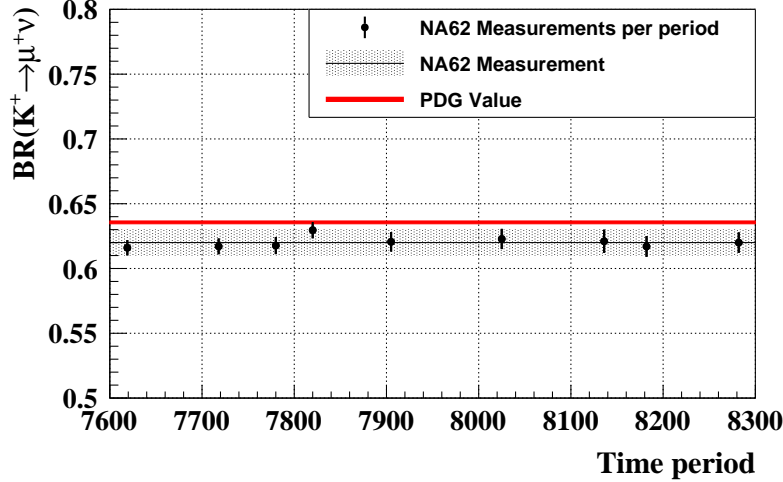


Figure 9: Measured branching ratio of the  $K^+ \rightarrow \mu^+ \nu$  decay mode in different time periods of the 2017 data taking. The overall quoted uncertainty is mostly systematic.

in agreement within 2.5% with the PDG value [7]. The 0.01 uncertainty is systematic, mainly attributable to the corrections described above. The statistical uncertainty is negligible. The result is stable within uncertainties when signal and normalization selection cuts are varied. It is also stable throughout the 2017 data taking, as shown in Figure 9.

This result relies on simulation to account for the different acceptances of the  $K^+ \rightarrow \mu^+ \nu$  and  $K^+ \rightarrow \pi^+ \pi^0$  decay modes, as in the case of the  $SES$  measurement. The comparison between the measured and PDG branching ratios is used to set the level of accuracy in the simulations, leading to a relative uncertainty of 2.5% being propagated to  $SES$ .

### 6.2.3 Random veto efficiency

In both  $K^+ \rightarrow \pi^+ \nu \bar{\nu}$  and  $K^+ \rightarrow \pi^+ \pi^0$  event selections, the GTK, CHANTI, STRAW, and MUV3 are also used to veto backgrounds. Data are used to estimate the fraction of kaon decays rejected due to accidental activity in these detectors. Measurements on samples of  $K^+ \rightarrow \pi^+ \pi^0$  and  $K^+ \rightarrow \mu^+ \nu$  show that the fraction of events accepted by each of these detectors is about 0.9, 0.97, 0.9, and 0.95. These veto requirements are uncorrelated and, in total, reject about 25% of signal and normalization decays. Because the average beam intensity of selected normalization and signal-like events is comparable, the effects of the GTK, CHANTI, STRAW and MUV3 vetoes cancel in the ratio of Equation (4).

The criteria, collectively termed *photon and multiplicity rejection* (section 5.6), employed to veto  $K^+$  decays with photons or more than one charged particle in the final state also reject signal events if accidental particles overlap the  $\pi^+$  in time.

The fraction of signal events passing photon and multiplicity rejection is denoted  $\epsilon_{RV}$  and called the *random veto efficiency*. A sample of  $K^+ \rightarrow \mu^+ \nu$  decays selected from minimum-bias data is used to estimate  $\epsilon_{RV}$ . The selection closely follows that of  $K^+ \rightarrow \pi^+ \nu \bar{\nu}$ , including GTK-, CHANTI-, and STRAW-based veto criteria, except that:  $|(P_K - P_\mu)^2| < 0.006 \text{ GeV}^2/c^4$  replaces the missing-mass squared regions; the calorimeters and the MUV3 are used for  $\mu^+$  identification; and no box cut or the photon and multiplicity rejection criteria are applied. Simulation shows that the background to  $K^+ \rightarrow \mu^+ \nu$  is less than a part per thousand.

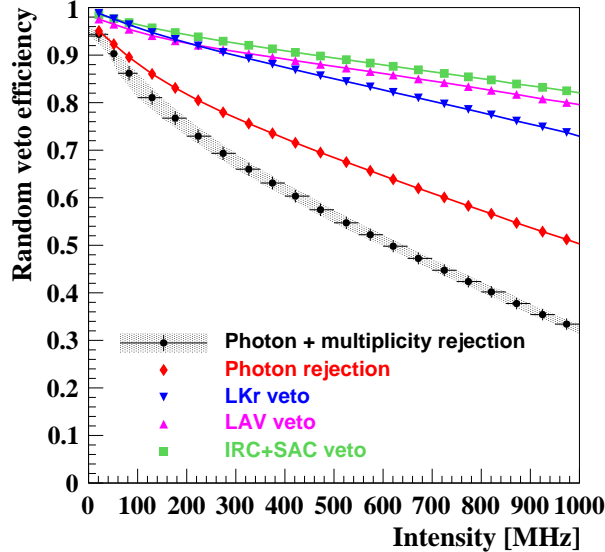


Figure 10: Random veto efficiency  $\epsilon_{RV}$  in bins of instantaneous beam intensity after photon and multiplicity rejection, after photon rejection, after LKr veto only, after LAV veto only, and after IRC and SAC veto only. The error bars on the photon and multiplicity rejection points indicates the total uncertainty. Lines are drawn as guides for the eye.

The random veto efficiency is computed as the ratio between the number of  $K^+ \rightarrow \mu^+ \nu$  events remaining before and after photon and multiplicity rejection. Figure 10 displays  $\epsilon_{RV}$  as a function of the instantaneous beam intensity. This result is corrected for the probability of event loss induced by  $\mu^+$  interactions, such as  $\delta$ -ray production in the RICH material, as estimated by simulation. This correction increases  $\epsilon_{RV}$  by about 1%. An uncertainty of 100% is assigned to this correction, leading to a 1% systematic uncertainty in  $\epsilon_{RV}$ . The stability of  $\epsilon_{RV}$  is tested against cuts on  $(P_K - P_\mu)^2$  and  $\mu^+$  identification. The maximum observed relative variation is 2.4% due to the cut on the calorimetric BDT probability. Half this variation is used to correct the measured  $\epsilon_{RV}$  and half is assigned as a systematic uncertainty. A residual dependence on the  $\mu^+$  momentum is observed and added to the total systematic uncertainty. The final average random veto efficiency is  $0.638 \pm 0.014$ . Table 3 summarizes the different contributions to the uncertainty.

Because the random veto affects only the signal, the uncertainty in  $\epsilon_{RV}$  contributes linearly to the uncertainty in the  $SES$ .

### 6.3 Trigger efficiency

Normalization events are selected from minimum-bias data, and signal events are selected from PNN data. Problems in the hardware and trigger definitions in conflict with offline cuts may cause the trigger to reject good normalization and signal events. Because minimum-bias and PNN triggers differ, their efficiencies, denoted  $\epsilon_{trig}^{MB}$  and  $\epsilon_{trig}^{PNN}$  in Equation (4), do not cancel in the ratio, which therefore must be precisely evaluated. The L0 and L1 trigger algorithms which identify signal candidates employ different sets of detectors, so their efficiencies can be studied separately.

Table 3: Contributions to the uncertainty of the random veto efficiency measurement. The total uncertainty is the sum in quadrature of the contributions.

Source	Uncertainty in $\epsilon_{RV}$
$\mu^+$ interaction correction	$\pm 0.011$
$\mu^+$ identification	$\pm 0.008$
Momentum dependence	$\pm 0.003$
Statistical uncertainty	$< 0.001$
Total	$\pm 0.014$

### 6.3.1 PNN L0 trigger efficiency

The L0 efficiency stems from conditions in the RICH, CHOD, and MUV3, termed L0NoCalo, and veto conditions in the LKr, called L0Calo. A sample of  $K^+ \rightarrow \pi^+\pi^0$  events selected from minimum-bias data using PNN-like criteria allows the measurement of the L0NoCalo efficiency. The contributions from the RICH and CHOD are also estimated with  $K^+ \rightarrow \mu^+\nu$  decays. The measured L0NoCalo efficiency is about 0.980 at the mean intensity of 450 MHz and varies almost linearly as a function of the instantaneous beam intensity, decreasing by about 1% at twice the mean intensity. The main source of inefficiency comes from the MUV3 veto criteria, because the veto timing window is larger online than offline due to online time resolution. The uncertainty in the measured value is at the level of 0.5%, is mostly systematic and reflects the deviation of the efficiency from linearity.

The L0Calo efficiency is measured with a sample of  $K^+ \rightarrow \pi^+\pi^0$  decays in which the two photons are detected in LAV stations. Events of this type result in a  $\pi^+$  with momentum greater than 45 GeV/c in the LKr. The L0Calo efficiency, defined as the fraction of events passing the L0Calo conditions, is measured as a function of the energy,  $E_{LKr}$ , that the  $\pi^+$  deposits in the LKr. The dependence on  $E_{LKr}$  is converted into a dependence on the  $\pi^+$  momentum,  $p_{\pi^+}$ , in the 15 – 35 GeV/c range, with a conversion factor extracted from the  $E_{LKr}/p_{\pi^+}$  distribution of a sample of  $\pi^+$ s selected from  $K^+ \rightarrow \pi^+\pi^+\pi^-$  decays. The L0Calo efficiency depends on the  $\pi^+$  momentum, and decreases from 0.965 to 0.910 between the first and the last momentum bin. The requirement that there be no more than 30 GeV detected in the LKr, convoluted with the energy resolution of the LKr, is the main source of inefficiency. The uncertainty in the L0Calo trigger efficiency comes from the statistics of the  $K^+ \rightarrow \pi^+\pi^+\pi^-$  sample used to map  $E_{LKr}$  into  $p_{\pi^+}$ .

The overall L0 trigger efficiency is the product of the L0NoCalo and L0Calo efficiencies as a function of  $\pi^+$  and intensity. The measured value decreases with both increasing  $\pi^+$  momentum and intensity, ranging from 0.95 to 0.9.

### 6.3.2 PNN L1 trigger efficiency

The effects of independent KTAG, LAV, and STRAW requirements in the L1 trigger efficiency are uncorrelated, such that the overall efficiency is the product of the individual efficiencies. Samples of  $K^+ \rightarrow \mu^+\nu$  selected from minimum-bias data and of  $K^+ \rightarrow \pi^+\pi^0$  selected from data triggered by the PNN L0 conditions and recorded irrespective of the L1 trigger decision were used to measure these efficiencies. The L1 trigger algorithms were emulated offline, including the effects of resolution.

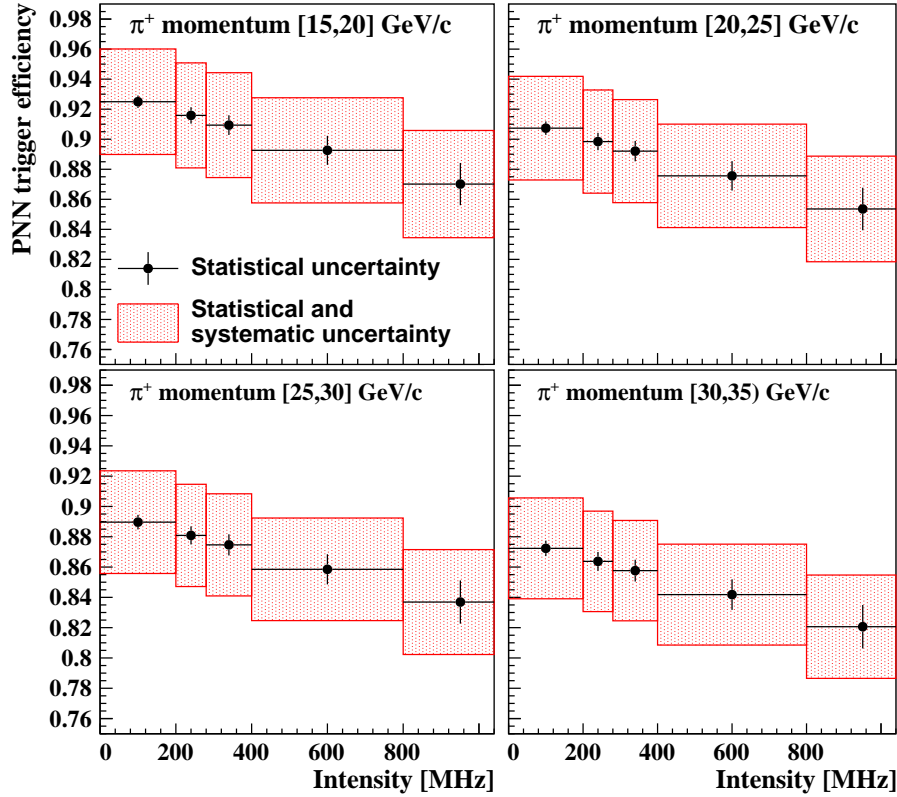


Figure 11: Measured PNN trigger efficiency as a function of instantaneous beam intensity in four bins of  $\pi^+$  momentum. The shaded band corresponds to the total uncertainty.

After applying PNN selection criteria, the KTAG L1 requirements do not introduce additional loss of signal. On the other hand, the LAV requirements introduce intensity-dependent losses of events which pass signal offline selection criteria, because the online LAV time resolution requires a larger veto timing window than that used offline. The L1 LAV efficiency in the first part of the 2017 data-taking period ranges from 0.965 to 0.955, depending on the intensity. This efficiency is about 1% higher and exhibits less intensity dependence in the second part of 2017 data taking as a consequence of an optimization of the L1 LAV algorithm. The spread of the efficiency among data-taking periods is used to set a systematic uncertainty for this measurement, which amounts to about 0.4% (1.4%) at low (high) intensity.

The efficiency of the L1 STRAW algorithm is greater than 0.99 and independent of intensity. A  $\pm 0.2\%$  uncertainty is assigned to this value to account for an observed  $\pi^+$  momentum dependence.

### 6.3.3 Trigger efficiency and *SES*

The effect of the trigger efficiency on the *SES* is determined using Equation (4) with the following assumptions: the total PNN trigger efficiency is the product of the L0 and L1 efficiencies; the efficiency of the L0TP is the same for the PNN and the minimum bias trigger and therefore

Table 4: Contributions to the uncertainty of the trigger efficiency. When quoted, the range corresponds to the efficiency dependence on the instantaneous beam intensity and the  $\pi^+$  momentum.

Source	Trigger efficiency uncertainty
L0NoCalo	$\pm 0.002$ to $\pm 0.004$
L0Calo	$\pm 0.003$ to $\pm 0.004$
L1 LAV	$\pm 0.004$ to $\pm 0.014$
L1 Straw	$\pm 0.002$
Global	$\pm 0.035$

cancels in Equation (4); and the minimum-bias trigger is 100% efficient.

The following test is performed to check the accuracy of these assumptions. The PNN selection, except  $\pi^+$  identification with the RICH, is applied to minimum-bias data, leading to  $N^{MB} = 701 \pm 26$  events in the  $\mu\nu$  region of the  $m_{\text{miss}}^2$  distribution. The expected number of PNN data in this region passing the same selection can be written, under the above assumptions, as:

$$N^{PNN}(\text{expected}) = D \cdot N^{MB} \cdot \epsilon_{L0}^{PNN} \cdot \epsilon_{L1}^{PNN}. \quad (8)$$

Here  $D$  is the minimum-bias reduction factor and  $\epsilon_{L0}^{PNN}$  ( $\epsilon_{L1}^{PNN}$ ) are the L0 (L1) PNN trigger efficiencies for  $K^+ \rightarrow \mu^+\nu$  decays in which the muon resembles a pion in the calorimeters and does not hit MUV3. Considering that  $K^+ \rightarrow \mu^+\nu$  decays are fully efficient under the L0Calo condition (section 6.3.1), the measured values of  $\epsilon_{L0}^{PNN}$  and  $\epsilon_{L1}^{PNN}$  lead to  $N^{PNN}(\text{expected}) = (263 \pm 10) \times 10^3$ . The number of PNN data observed in the  $\mu\nu$  region of the  $m_{\text{miss}}^2$  distribution after removing the RICH identification from the PNN selection is  $N^{PNN}(\text{observed}) = (255.6 \pm 0.6) \times 10^3$ , in agreement within  $\pm 3.8\%$  with  $N^{PNN}(\text{expected})$ . This value is assigned as systematic uncertainty to the measured PNN trigger efficiency (noted Global in Table 4).

The PNN trigger efficiency relevant to the measurement of  $SES$  is shown in Figure 11 as a function of instantaneous beam intensity and  $\pi^+$  momentum. The overall average trigger efficiency is  $0.87 \pm 0.03$ . Table 4 summarizes the various contribution to the uncertainty in the trigger efficiency.

## 6.4 $SES$ result

The single event sensitivity and the total number of expected Standard Model  $K^+ \rightarrow \pi^+\nu\bar{\nu}$  decays are:

$$SES = (0.389 \pm 0.024_{\text{sys}}) \times 10^{-10}, \quad (9)$$

$$N_{\pi\nu\bar{\nu}}^{\text{exp}}(SM) = 2.16 \pm 0.13_{\text{sys}} \pm 0.26_{\text{ext}}. \quad (10)$$

The statistical uncertainty is negligible. Table 5 details the various contributions to the  $SES$ , averaged over instantaneous beam intensity and  $\pi^+$  momentum. This list of contributions is for reference only, as the measured value of the  $SES$  comes from Equation (4) in bins of instantaneous beam intensity and  $\pi^+$  momentum.

The above  $SES$  corresponds to about  $1.5 \times 10^{12}$  effective  $K^+$  decays in the FV, defined as  $(D \cdot N_{\pi\pi}) / (\epsilon_{\pi^+\pi^0}^{MC} \cdot \text{BR}(K^+ \rightarrow \pi^+\pi^0))$ . This quantity is proportional to the actual number of  $K^+$

Table 5: Contributions to  $SES$ , averaged over instantaneous beam intensity and  $\pi^+$  momentum.

Contribution	value
$N_{\pi\pi}$	$68 \times 10^6$
$K^+ \rightarrow \pi^+\nu\bar{\nu}$ Monte Carlo efficiency, $\epsilon_{\pi\nu\nu}^{MC}$	$0.030 \pm 0.003$
$K^+ \rightarrow \pi^+\pi^0$ Monte Carlo efficiency, $\epsilon_{\pi^+\pi^0}^{MC}$	$0.087 \pm 0.009$
Random veto efficiency (photon and multiplicity rejection)	$0.638 \pm 0.014$
Trigger efficiency	$0.87 \pm 0.03$

decays in the FV, although not strictly equal because  $\epsilon_{\pi^+\pi^0}^{MC}$  does not include the elements which factor out and cancel in Equation (4).

Table 6 lists the different sources of  $SES$  uncertainty, including contributions to the uncertainty of the Monte Carlo and trigger efficiency ratios, as discussed in sections 6.2 and 6.3, respectively. The external error on  $N_{\pi\nu\nu}^{exp}$  stems from the uncertainty in the theoretical prediction of  $\text{BR}(K^+ \rightarrow \pi^+\nu\bar{\nu})$ . Figure 12 shows  $N_{\pi\nu\nu}^{exp}$  in bins of  $\pi^+$  momentum and instantaneous beam intensity.

Table 6: Sources contributing to the uncertainty in the  $SES$  measurement. “Normalization background” refers to the impact of  $K^+ \rightarrow \pi^+\pi^0$  decays on the normalization sample. The total uncertainty is the sum in quadrature of the four contributions listed in the first column.

Source	Uncertainty in $SES$ ( $\times 10^{10}$ )
Monte Carlo efficiency ratio	$\pm 0.017$
$\pi^+$ interactions	$\pm 0.012$
RICH reconstruction	$\pm 0.006$
$m_{\text{miss}}^2$ Selection	$\pm 0.004$
Acceptance simulation	$\pm 0.010$
Trigger efficiency	$\pm 0.015$
L0 Efficiency	$\pm 0.002$
L1 Efficiency	$\pm 0.003$
Global	$\pm 0.015$
Random Veto efficiency	$\pm 0.008$
Normalization Background	$< 0.001$
Total	$\pm 0.024$

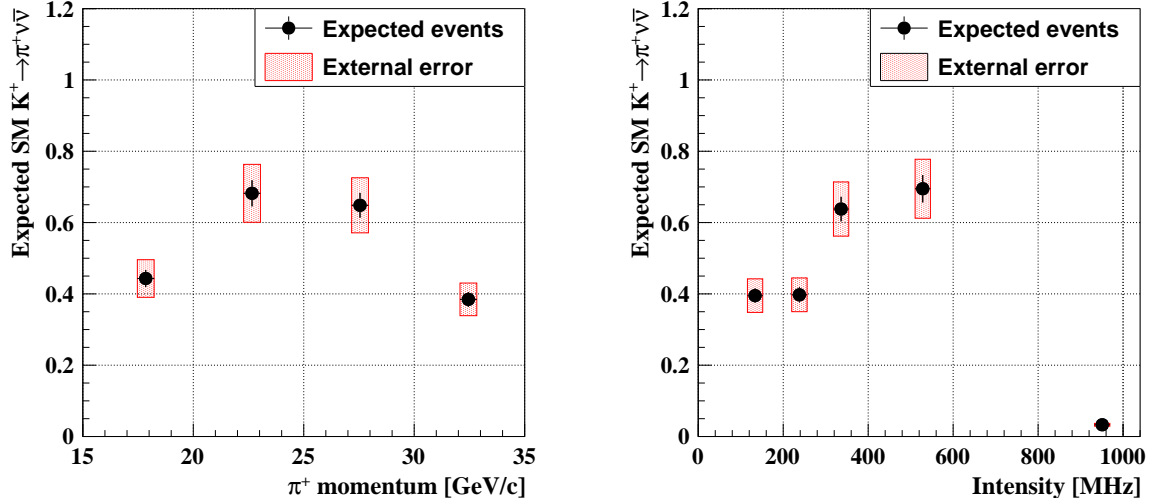


Figure 12: Number of expected Standard Model  $K^+ \rightarrow \pi^+ \nu \bar{\nu}$  events in bins of  $\pi^+$  momentum (left) and average beam intensity (right). The average beam intensity per bin, obtained from the  $K^+ \rightarrow \pi^+ \pi^0$  sample used for normalization, is plotted at the barycentre of the bin.

## 7 Expected background

The background to  $K^+ \rightarrow \pi^+ \nu \bar{\nu}$  decays can be divided into two classes. The  $K^+$  decay background is due to kaon decays in the FV other than  $K^+ \rightarrow \pi^+ \nu \bar{\nu}$ , while the upstream background is due to  $\pi^+$  particles produced either by beam particle interactions or by kaon decays upstream of the FV. To mimic a signal, a background event should have a  $K^+$  reconstructed upstream and matched to a  $\pi^+$  downstream, and  $m_{\text{miss}}^2$  reconstructed in the signal region. Furthermore, either the extra particles produced in association with the  $\pi^+$  should escape detection, or a lepton in the final state should be mis-identified as a  $\pi^+$ .

### 7.1 $K^+$ decay background

The background from  $K^+$  decays in the FV is primarily due to the  $K^+ \rightarrow \pi^+ \pi^0$ ,  $K^+ \rightarrow \mu^+ \nu$ ,  $K^+ \rightarrow \pi^+ \pi^+ \pi^-$  and  $K^+ \rightarrow \pi^+ \pi^- e^+ \nu$  decays.

The first three processes are constrained kinematically, and enter the signal regions via  $m_{\text{miss}}^2$  mis-reconstruction due to large-angle Coulomb scattering, elastic hadronic interactions in GTK and STRAW material, incorrect  $K/\pi$  association, pattern recognition errors, or position mis-measurement in the spectrometers. In addition to  $m_{\text{miss}}^2$  mis-reconstruction, at least one of the following should occur: photons from a  $K^+ \rightarrow \pi^+ \pi^0$  decay are not detected by electromagnetic calorimeters; the muon from a  $K^+ \rightarrow \mu^+ \nu$  decay is mis-identified as  $\pi^+$  by the RICH counter, hadronic calorimeters and MUV3; a  $\pi^+ \pi^-$  pair from a  $K^+ \rightarrow \pi^+ \pi^+ \pi^-$  decay is undetected by the STRAW and the other downstream detectors.

The background from the three kinematically-constrained decays is evaluated with data. Denoting by  $N_{\text{decay}}$  the number of events in the corresponding background region of  $m_{\text{miss}}^2$  in the PNN data sample passing the PNN selection, and by  $f_{\text{kin}}$  the probability that  $m_{\text{miss}}^2$  is reconstructed in the signal region, the expected number of background events from each decay is given by

$$N_{\text{decay}}^{\text{exp}} = N_{\text{decay}} \cdot f_{\text{kin}}. \quad (11)$$

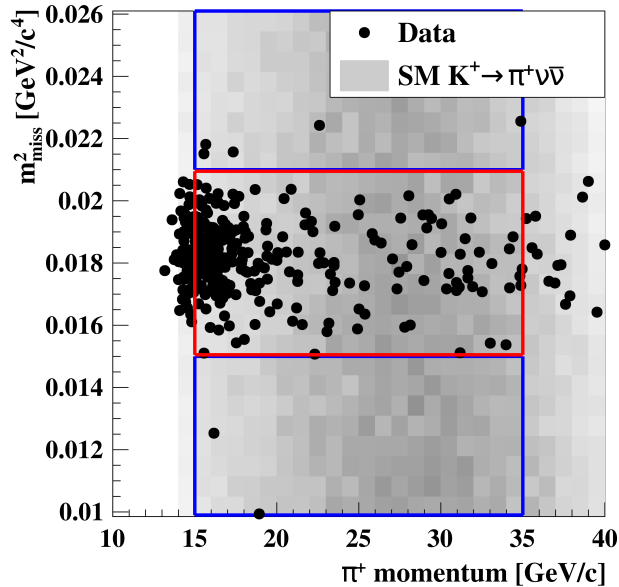


Figure 13: Distribution of the PNN events in the  $(\pi^+$  momentum,  $m_{\text{miss}}^2$ ) plane after the PNN selection in the  $\pi^+\pi^0$  (red box) and control  $m_{\text{miss}}^2$  regions (blue boxes). Both control regions are used only for validation of the background estimation. The shaded grey area represents the distribution of the simulated SM  $K^+ \rightarrow \pi^+\nu\bar{\nu}$  events (arbitrarily normalized).

The value of  $N_{\text{decay}}$  is obtained directly from the PNN data, while the probability  $f_{\text{kin}}$  is measured with minimum-bias data. This technique does not require knowledge of photon and charged particle rejection inefficiencies or of the  $\pi^+$  mis-identification probability. Nevertheless, the precision of the method relies on three assumptions whose reasonableness is tested with both data and simulations:

1.  $f_{\text{kin}}$  represents the probability that an event of a given decay mode enters the signal region;
2.  $f_{\text{kin}}$  and  $N_{\text{decay}}$  are uncorrelated; and
3.  $N_{\text{decay}}$  accounts only for events of the corresponding decay mode.

Backgrounds from the  $K^+ \rightarrow \pi^+\pi^-e^+\nu$  decay, as well as from the rare decay  $K^+ \rightarrow \pi^+\gamma\gamma$  and the semileptonic decays  $K^+ \rightarrow \pi^0\ell^+\nu$  ( $\ell = e, \mu$ ), are evaluated with simulations.

In the following subsections the  $K^+ \rightarrow \pi^+\pi^0$  and the  $K^+ \rightarrow \mu^+\nu$  backgrounds are shown in bins of  $\pi^+$  momentum up to 40 GeV/c, albeit only the 15–35 GeV/c momentum range is used to evaluate the corresponding backgrounds in the signal regions.

### 7.1.1 $K^+ \rightarrow \pi^+\pi^0$ decay

After the PNN selection,  $N_{\pi\pi} = 264$  events from the PNN sample remain in the  $\pi^+\pi^0$  region. The distribution of these events in the  $(\pi^+$  momentum,  $m_{\text{miss}}^2$ ) plane is shown in Figure 13, after the unblinding of the  $K^+ \rightarrow \pi^+\pi^0$  control regions. The  $\pi^+$  momentum lies in the 15–20 GeV/c range for 60% of these events, due to the degradation of the  $\pi^0$  detection efficiency for photons emitted at small angles (section 5.6). The measurement of  $f_{\text{kin}}$  is based on a  $K^+ \rightarrow \pi^+\pi^0$  sample selected from minimum-bias data. The selection involves the  $K^+ \rightarrow \pi^+$  decay definition



described in sections 5.1, 5.2 and 5.5. The conditions of section 5.3 are applied as well, however the decay region is defined as  $115 < Z_{\text{vertex}} < 165$  m. Specific selection criteria are employed to tag the  $\pi^0$  by reconstructing two photons from the  $\pi^0 \rightarrow \gamma\gamma$  decay in the LKr calorimeter independently of the  $\pi^+$  and  $K^+$  tracks. The quantity  $Z_{\text{vertex}}$  is evaluated from the coordinates of the two photon energy clusters in LKr by assuming that they originate from a  $\pi^0$  decay on the nominal beam axis. The vertex is required to be within the decay region, and its position is used to reconstruct the photon and the  $\pi^0$  momenta. Consequently, the expected  $\pi^+$  trajectory is reconstructed and is required to be in the geometric acceptance of the detectors. The reconstructed squared missing mass  $(P_K - P_0)^2$ , where  $P_K$  and  $P_0$  are the four-momenta of the nominal  $K^+$  and the reconstructed  $\pi^0$ , peaks at the squared  $\pi^+$  mass for  $K^+ \rightarrow \pi^+\pi^0$  decays. A cut on this quantity is applied to select an almost background-free  $K^+ \rightarrow \pi^+\pi^0$  sample without biasing the  $m_{\text{miss}}^2$  reconstruction.

Figure 14 (top left) displays the  $m_{\text{miss}}^2$  spectrum of the  $K^+ \rightarrow \pi^+\pi^0$  minimum-bias sample used for  $f_{\text{kin}}$  measurement:  $f_{\text{kin}}$  is evaluated for each of the signal regions 1 and 2 as the ratio of the numbers of events in the signal region and in the  $K^+ \rightarrow \pi^+\pi^0$  region. The simulation reproduces the tails within the statistical uncertainties, and the background is negligible. The measured values of  $f_{\text{kin}}$  in bins of  $\pi^+$  momentum are shown in Figure 14 (bottom left). Incorrect  $K/\pi$  association due to the pileup in the GTK accounts for 50% of the contribution to  $f_{\text{kin}}$  in region 1, and 30% in region 2.

The total expected background in the signal regions, evaluated by applying Equation (11) in each  $\pi^+$  momentum bin, is  $N_{\pi\pi}^{\text{exp}} = 0.27 \pm 0.026_{\text{stat}} \pm 0.014_{\text{syst}}$ . The statistical uncertainty is mainly due to  $N_{\pi\pi}$ . The systematic uncertainty accounts for a possible bias to the shape of the  $m_{\text{miss}}^2$  spectrum induced by the  $\pi^0$  tagging used to measure  $f_{\text{kin}}$ . It is evaluated by comparing the simulated shape of the  $m_{\text{miss}}^2$  spectrum in the minimum-bias sample with that of  $K^+ \rightarrow \pi^+\pi^0$  decays used for normalization (Figure 14, top right). The 5% difference between the numbers of events in region 1 in the two samples is taken as a systematic uncertainty.

Radiative decays in the simulated  $K^+ \rightarrow \pi^+\pi^0$  sample are modeled according to [26]. Simulation studies show that decays with radiative photons energetic enough to shift the reconstructed  $m_{\text{miss}}^2$  value to the signal regions are absent in the minimum-bias sample, due to the  $\pi^0$  tagging suppression (Figure 14 top right). However the presence of an additional photon in the final state improves the photon veto, compensating for the weaker kinematic suppression. The contribution of the radiative component to the  $K^+ \rightarrow \pi^+\pi^0$  decays is computed by applying the measured single photon detection efficiency (section 5.6) to the simulated  $K^+ \rightarrow \pi^+\pi^0$  decays entering signal region 2 because of the presence of radiated photons. It is concluded that the presence of an additional photon improves the rejection of  $K^+ \rightarrow \pi^+\pi^0$  in region 2 by a factor of almost 30 with respect to the case of the photons from the  $\pi^0$  decay only. This leads to an increase of the expected  $K^+ \rightarrow \pi^+\pi^0$  background of 0.02 events. A systematic uncertainty of 100% is conservatively considered for this value, mainly due to the accuracy of the simulation and the modelling of the single photon detection efficiency.

The numbers of expected  $K^+ \rightarrow \pi^+\pi^0$  events in the signal regions are presented in Table 7. The overall background expected in the signal regions, including the effect of the radiative decays, is

$$N_{\pi\pi}^{\text{exp}} = 0.29 \pm 0.03_{\text{stat}} \pm 0.03_{\text{syst}}. \quad (12)$$

To validate this result, the numbers of expected and observed events are compared in the two  $\pi^+\pi^0$  control regions. The probability  $f_{\text{kin}}$  for the control regions is measured to be about 25 times higher than for the corresponding signal regions, and the expected background scales accordingly. The contribution from radiative decays in control regions is found negligible. Table 7 and in Figure 14 (bottom right) present the numbers of expected and observed events in the control regions, found to be in good agreement. The uncertainties in the expected background in the control regions are mostly systematic due to the modelling of the  $m_{\text{miss}}^2$  spectrum.

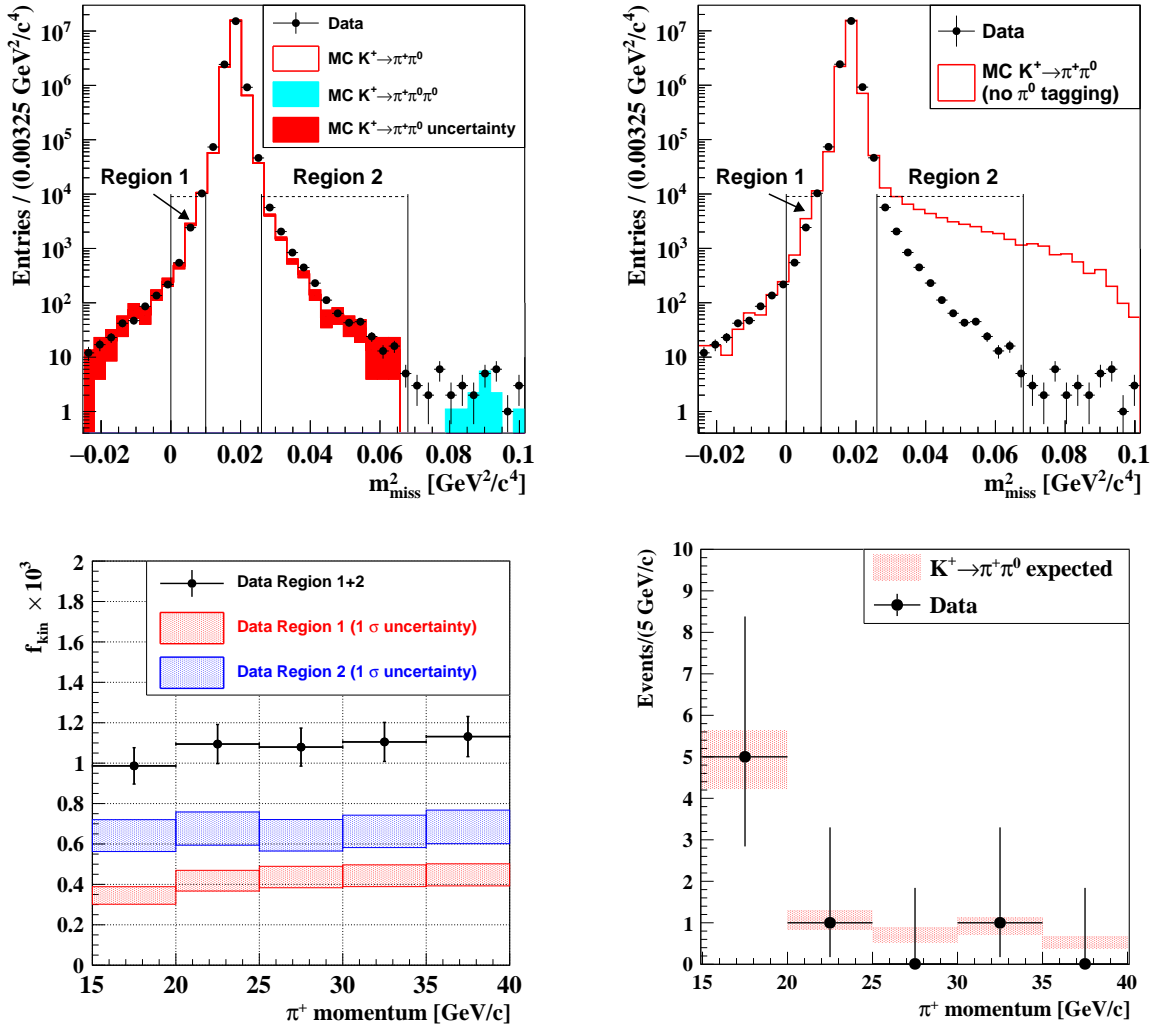


Figure 14: **Top left**: reconstructed  $m_{\text{miss}}^2$  distribution of the  $K^+ \rightarrow \pi^+\pi^0$  minimum-bias data events selected by tagging the  $\pi^0$  (full symbols, see text for details) integrated over the 15 – 35 GeV/c momentum range. Simulated samples of  $K^+ \rightarrow \pi^+\pi^0$  decays and backgrounds (normalized to the data in the  $K^+ \rightarrow \pi^+\pi^0$  region) are superimposed. Signal regions 1 and 2 are shown. The  $K^+ \rightarrow \pi^+\pi^0$  region, defined by the condition  $0.015 < m_{\text{miss}}^2 < 0.021 \text{ GeV}^2/c^4$ , and the control regions, comprised between the signal and  $K^+ \rightarrow \pi^+\pi^0$  regions, are not shown. **Top right**: same as top-left, but the simulated  $K^+ \rightarrow \pi^+\pi^0$  sample is selected without applying the  $\pi^0$  tagging; simulated backgrounds are not shown. **Bottom left**: the probability  $f_{\text{kin}}$ , defined in the text, measured using the  $K^+ \rightarrow \pi^+\pi^0$  minimum-bias sample in bins of  $\pi^+$  momentum, separately for signal region 1 and 2 and combined, with the statistical uncertainties. **Bottom right**: expected and observed numbers of background events in the  $K^+ \rightarrow \pi^+\pi^0(\gamma)$  decay control regions in  $\pi^+$  momentum bins. The errors are statistical for the observed numbers of events, and dominated by systematics for the expected numbers of events.

Table 7: Expected numbers of  $K^+ \rightarrow \pi^+\pi^0$  events in the signal regions, and expected and observed numbers of events in the control regions. “Control region 1” corresponds to  $0.010 < m_{\text{miss}}^2 < 0.015 \text{ GeV}^2/c^4$ , “Control region 2” to  $0.021 < m_{\text{miss}}^2 < 0.026 \text{ GeV}^2/c^4$ . Expected events in both signal and control regions 2 are corrected for the contribution from the radiative component of the decay. The uncertainties are the sums in quadrature of the statistical and systematic ones. Radiative decays are kinematically forbidden in both signal region 1 and control region 1.

Region	Expected $K^+ \rightarrow \pi^+\pi^0$	Observed
Signal region 1	$0.11 \pm 0.01$	masked
Signal region 2	$0.18 \pm 0.04$	masked
Control region 1	$2.6 \pm 0.3$	2
Control region 2	$5.2 \pm 0.6$	5

Table 8: Number of PNN-triggered events that pass the PNN selection and are reconstructed in the  $\mu\nu$  region, observed in the data in bins of  $\pi^+$  momentum.

Momentum bins (GeV/c)	15 – 20	20 – 25	25 – 30	30 – 35
Observed events	1	48	143	287

### 7.1.2 $K^+ \rightarrow \mu^+\nu$ decay

After the PNN selection,  $N_{\mu\nu} = 479$  events from the PNN sample remain in the  $\mu\nu$  region. The numbers of events in bins of reconstructed  $\pi^+$  momentum are presented in Table 8, and the distribution of these events in the ( $\pi^+$  momentum,  $m_{\text{miss}}^2$ ) plane is shown in Figure 15 (top left). The momentum dependence is a consequence of the  $K^+ \rightarrow \mu^+\nu$  kinematics when the  $\pi^+$  mass is used to reconstruct  $m_{\text{miss}}^2$  and of the better performance of the RICH in rejecting  $\mu^+$  at low momentum. The background to  $N_{\mu\nu}$  is negligible.

Two methods are exploited to estimate the  $K^+ \rightarrow \mu^+\nu$  background.

In the first one, the measurement of  $f_{\text{kin}}$  is based on a  $K^+ \rightarrow \mu^+\nu$  sample selected from minimum-bias data, as described in sections 5.1 and 5.2. Additionally, the calorimetric BDT probability must be consistent with the identification of a  $\mu^+$ , while events are discarded if the STRAW track is identified as  $\pi^+$  or  $e^+$  in the calorimeters. The decay region is defined as  $115 < Z_{\text{vertex}} < 165 \text{ m}$ . The rejection of photons and extra charged particles is the same as in the PNN selection (section 5.6). The box cut and the kinematic requirements on  $m_{\text{miss}}^2$  are not applied. Figure 15 (top right) displays the  $m_{\text{miss}}^2$  spectrum of the  $K^+ \rightarrow \mu^+\nu$  minimum-bias sample used for  $f_{\text{kin}}$  measurement:  $f_{\text{kin}}$  is evaluated for each of the signal regions 1 and 2 as the ratio of the numbers of events in the signal and  $\mu\nu$  regions. The signal region definition does not include the cuts on  $m_{\text{miss}}^2$  computed using the momentum evaluated from the RICH information. Simulation reproduces the shape of the  $m_{\text{miss}}^2$  spectrum within the statistical uncertainties, and the background is negligible. The measured  $f_{\text{kin}}$  values in bins of reconstructed  $\pi^+$  momentum are shown in Figure 15 (bottom left). At large momentum,  $f_{\text{kin}}$  increases because the  $m_{\text{miss}}^2$  of  $K^+ \rightarrow \mu^+\nu$  events computed assuming the  $\pi^+$  mass approaches signal region 1. Simulations show

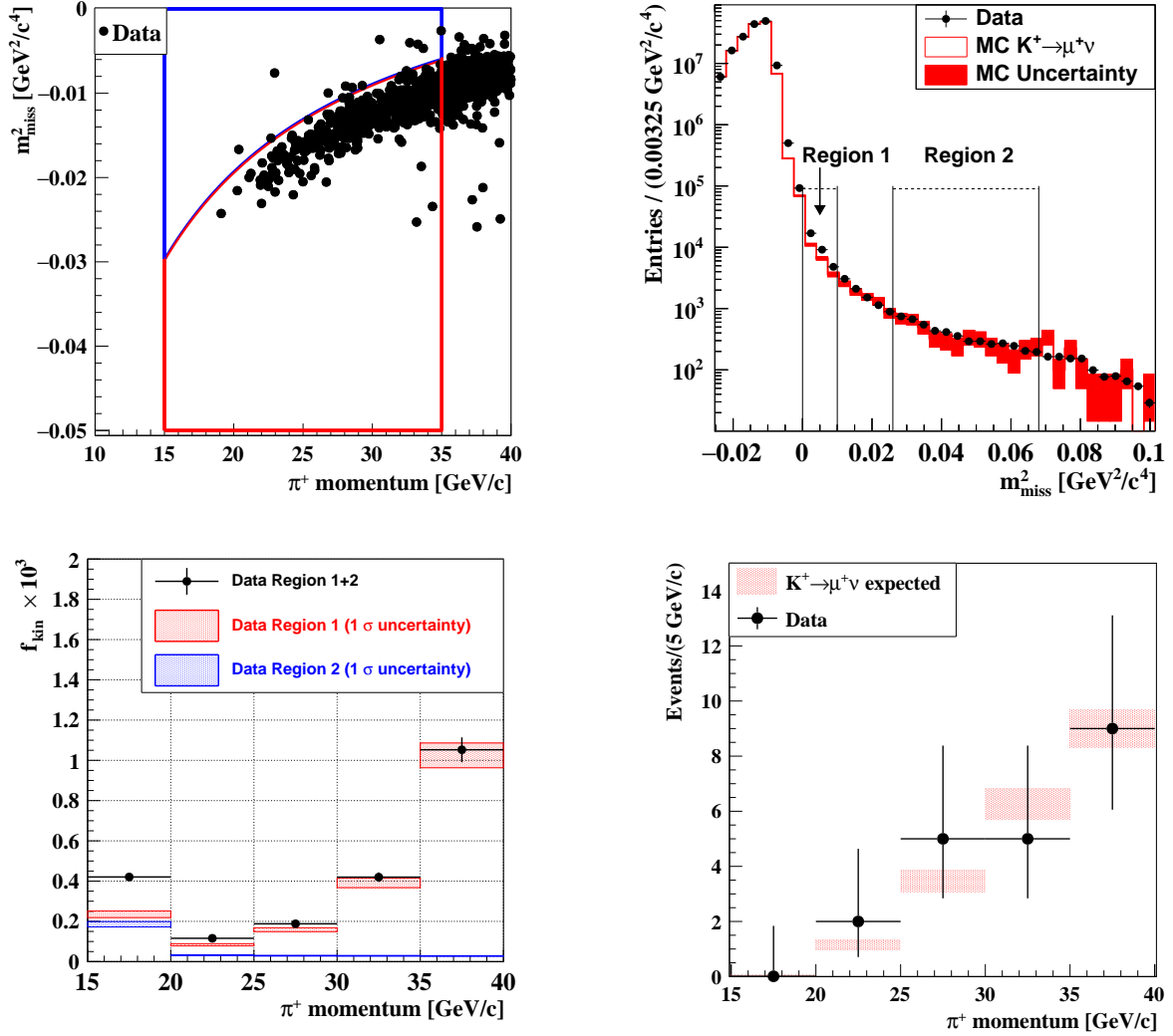


Figure 15: **Top left:** distributions of the PNN-triggered events in the  $(\pi^+$  momentum,  $m_{\text{miss}}^2$ ) plane after the PNN selection in the  $\mu\nu$  (red contour) and control  $m_{\text{miss}}^2$  (blue contour) regions. The control region is used only for validation of the background estimation. **Top right:** reconstructed  $m_{\text{miss}}^2$  distribution of the  $K^+ \rightarrow \mu^+ \nu$  minimum-bias data events (full symbols, see text for details) integrated over the 15–35 GeV/c momentum range. The distribution of simulated  $K^+ \rightarrow \mu^+ \nu$  decays is superimposed. Signal regions 1 and 2 are shown. **Bottom left:** the probability  $f_{\text{kin}}$  measured using the  $K^+ \rightarrow \mu^+ \nu$  minimum-bias sample in bins of reconstructed  $\pi^+$  momentum, separately for signal region 1 and 2 and combined (black symbols), and the corresponding statistical uncertainties. **Bottom right:** expected and observed numbers of background events from  $K^+ \rightarrow \mu^+ \nu$  decays in the  $\mu\nu$  control region in  $\pi^+$  momentum bins. The errors are statistically dominated.

Table 9: Expected numbers of  $K^+ \rightarrow \mu^+\nu$  events in signal regions, and numbers of expected and observed events in the control region. The uncertainties are the sums in quadrature of the statistical and systematic ones.

Region	Expected $K^+ \rightarrow \mu^+\nu$	Expected $K^+ \rightarrow \mu^+\nu, \mu^+ \rightarrow e^+\nu\bar{\nu}$	Observed
Signal region 1	$0.11 \pm 0.04$	$0.04 \pm 0.02$	masked
Signal region 2	$< 0.005$	$< 0.005$	masked
Control region	$10.5 \pm 1.0$	$0.5 \pm 0.2$	12

that the contribution to  $f_{\text{kin}}$  due to incorrect  $K/\pi$  association is sub-dominant with respect to material effects. The total expected background in the signal region, evaluated with this method by applying Equation (11) in each  $\pi^+$  momentum bin, is  $N_{\mu\nu}^{\text{exp}} = 0.14 \pm 0.007_{\text{stat}} \pm 0.007_{\text{syst}}$ . The statistical uncertainty is due to  $N_{\mu\nu}$ . The systematic uncertainty comes from the stability of the result with the variation of the BDT probability cut, and accounts for a possible bias on  $f_{\text{kin}}$  due to the  $\mu^+$  identification criteria applied in the selection of the  $K^+ \rightarrow \mu^+\nu$  minimum-bias sample. This result relies on the assumption that the  $\pi^+$  identification with the RICH and the shape of the  $m_{\text{miss}}^2$  spectrum are uncorrelated. This assumption, in principle, is violated because  $K^+ \rightarrow \mu^+\nu$  events may enter the signal region due to track mis-reconstruction, which also affects particle identification with the RICH. In addition, the background estimation procedure does not include the cut on  $m_{\text{miss}}^2$  computed using the RICH to measure  $f_{\text{kin}}$ , which can bias the result.

To investigate the accuracy of these approximations, a second method is employed to evaluate the  $K^+ \rightarrow \mu^+\nu$  background. In this case the strategy is similar to that previously discussed, but the  $\pi^+$  identification by the RICH is removed from the PNN selection used to derive  $N_{\mu\nu}$  and added to the selection of the  $K^+ \rightarrow \mu^+\nu$  minimum-bias sample used to measure  $f_{\text{kin}}$ . In addition, the determination of  $f_{\text{kin}}$  includes the cuts on  $m_{\text{miss}}^2$  computed using the  $\pi^+$  momentum measured from the RICH in the  $\pi^+$  hypothesis. The  $\mu^+$  rejection by the RICH suppresses  $f_{\text{kin}}$  by two orders of magnitude with respect to that of Figure 15 (bottom left), keeping a similar dependence on the  $\pi^+$  momentum. This translates into a statistical uncertainty of 20% on  $f_{\text{kin}}$ . The expected background in the signal region is evaluated to be  $N_{\mu\nu}^{\text{exp}} = 0.08 \pm 0.02_{\text{stat}}$ . This method is free from the bias of the first method, as it relies only on the assumption that  $\mu^+$  rejection with the RICH and the calorimeters are uncorrelated. Simulations show that this assumption is valid as long as the  $\mu^+$  does not decay upstream of the RICH.

The average of the estimates of  $N_{\mu\nu}^{\text{exp}}$  from the two methods is used, and a systematic uncertainty equal to half of the difference ( $\pm 0.03$ ) is assigned to account for a possible bias due to the correlation between particle identification and shape of the  $m_{\text{miss}}^2$  spectrum. This background estimate includes also the contribution from the radiative component of the  $K^+ \rightarrow \mu^+\nu$  decays, as radiative decays enter the  $K^+ \rightarrow \mu^+\nu$  minimum-bias sample used to evaluate  $f_{\text{kin}}$ .

The background from muon decays in flight  $\mu^+ \rightarrow e^+\nu\bar{\nu}$  is not included in the above estimate (as  $f_{\text{kin}}$  is measured requiring muon identification), and is determined separately using simulation. The rejection of this background depends on the muon decay position within the detector setup. Decays in the FV affect the kinematics, however, positrons are efficiently rejected by particle identification. Decays within the STRAW spectrometer impact both kinematics and particle identification in the RICH, while decays downstream of the STRAW affect particle identification only. Simulations show that only  $\mu^+$  decays between the third and fourth STRAW chambers are relevant, leading to a worsening of both  $K^+ \rightarrow \mu^+\nu$  kinematics and particle

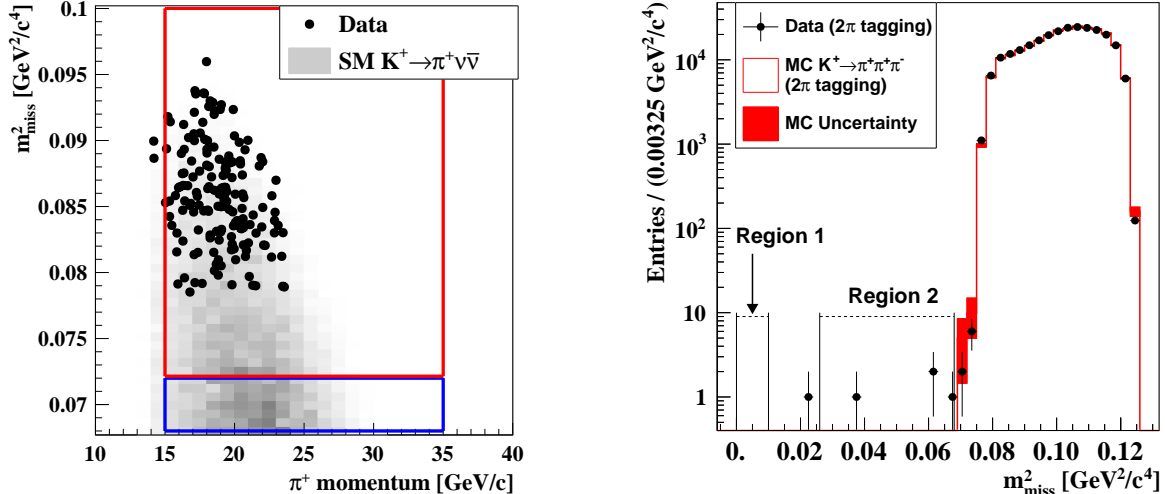


Figure 16: **Left:** distribution of the PNN-triggered events in the  $(\pi^+$  momentum,  $m_{\text{miss}}^2$ ) plane after the PNN selection in the  $3\pi$  (red box) and control  $m_{\text{miss}}^2$  regions (blue box). No event is found in the control region. The shaded grey area represents the distribution of the simulated SM  $K^+ \rightarrow \pi^+ \nu \bar{\nu}$  events (arbitrarily normalized). **Right:** reconstructed  $m_{\text{miss}}^2$  distribution for the unpaired  $\pi^+$  from  $K^+ \rightarrow \pi^+ \pi^+ \pi^-$  decays, obtained using the  $2\pi$  tagging method, selected from minimum-bias data and simulated samples. Signal regions 1 and 2 are shown.

identification. The background is found to contribute to region 1 only, and is computed to be  $0.04 \pm 0.02$ . The uncertainty quoted includes statistical and systematic contributions of similar magnitudes. The latter is evaluated by checks performed on data to validate the simulation of the positron rejection.

The numbers of expected  $K^+ \rightarrow \mu^+ \nu$  events in the signal regions are presented in Table 9. The overall background expected is

$$N_{\mu\nu}^{\text{exp}} = 0.15 \pm 0.02_{\text{stat}} \pm 0.04_{\text{syst}}, \quad (13)$$

with the contributions to the statistical and systematic uncertainties detailed above.

To validate this result, the numbers of expected and observed events are compared in the  $\mu\nu$  control region. The expected number of events is evaluated with a technique similar to that described above. This comparison is presented in Table 9 and Figure 15 (bottom right), showing good agreement between expected and observed numbers of events.

### 7.1.3 $K^+ \rightarrow \pi^+ \pi^+ \pi^-$ decay

After the PNN selection,  $N_{3\pi} = 161$  events from the PNN sample remain in the  $3\pi$  region. The distribution of these events in the  $(\pi^+$  momentum,  $m_{\text{miss}}^2$ ) plane is shown in Figure 16 (left); the  $\pi^+$  momentum is constrained kinematically to the region below 25 GeV/c.

The measurement of  $f_{\text{kin}}$  is based on a  $K^+ \rightarrow \pi^+ \pi^+ \pi^-$  sample selected from minimum-bias data. For this purpose, a  $\pi^+ \pi^-$  pair is used to tag the  $K^+ \rightarrow \pi^+ \pi^+ \pi^-$  decay without biasing the reconstruction of the unpaired  $\pi^+$ . The  $\pi^+$  to be paired to the  $\pi^-$  is chosen randomly event by event. The presence of a two-track vertex in the FV is required, and the quantity  $(P_{\pi^+} + P_{\pi^-} - P_{K^+})^2$ , where  $P_{\pi^\pm}$  are the reconstructed 4-momenta of the  $\pi^\pm$  and  $P_{K^+}$  is the nominal

kaon 4-momentum, must be consistent with the squared  $\pi^+$  mass. The selection proceeds with respect to the unpaired  $\pi^+$  as described in sections 5.1 and 5.2. Photon veto conditions are applied to the LAV, IRC and SAC only. The box cut, the kinematic cuts on  $m_{\text{miss}}^2$  and the multiplicity rejection are not applied.

The reconstructed  $m_{\text{miss}}^2$  spectra for the tagged unpaired  $\pi^+$  for the minimum-bias data and simulated samples are shown in Figure 16 (right). It is found that  $f_{\text{kin}} = (1.6_{-1.0}^{+2.0}) \times 10^{-5}$ , where the uncertainties are statistical. Data and simulations are consistent within the uncertainties.

The kinematics of the tagged  $\pi^+$  differs from that of the  $\pi^+$  remaining after the PNN selection, potentially biasing the  $f_{\text{kin}}$  measurement. In particular, the  $m_{\text{miss}}^2$  spectrum of the tagged sample does not match the one of the residual events in the  $3\pi$  region. The impact on the  $f_{\text{kin}}$  measurement is evaluated with simulations, varying the selection criteria. The full PNN selection cannot be applied to the simulated samples due to statistical limitations. Modified PNN selections used for the tests include those without the tagging, and with requirements of at least one and exactly one  $\pi^+$  reconstructed in the geometric acceptance. The latter selection is the most PNN-like, and leads to a shape of the  $m_{\text{miss}}^2$  spectrum in the  $3\pi$  region matching that of the data events passing the full PNN selection. The values of  $f_{\text{kin}}$  obtained from simulations with the modified selections are in agreement within the uncertainties quoted above.

A possible bias comes from the dependence of  $f_{\text{kin}}$  on the  $Z$ -position of the decay vertex, as the tagging affects the shape of the  $Z_{\text{vertex}}$  spectrum. To quantify this effect,  $f_{\text{kin}}$  is evaluated in bins of  $Z_{\text{vertex}}$  for data and simulated samples. The variation of  $f_{\text{kin}}$  across  $Z_{\text{vertex}}$  bins in simulated samples is conservatively considered as a systematic uncertainty. The final result is  $f_{\text{kin}} = (5 \pm 5) \times 10^{-5}$ .

The background computed using Equation (11) is

$$N_{3\pi} = 0.008 \pm 0.008. \quad (14)$$

To validate this result, the numbers of expected and observed events are compared in the (unmasked)  $3\pi$  control region. The expected number of events in the control region is sensitive to the shape of the  $m_{\text{miss}}^2$  spectrum close to the kinematic threshold of the  $K^+ \rightarrow \pi^+\pi^+\pi^-$  decay. Simulation studies lead to a conservative upper limit of  $1.5 \times 10^{-3}$  on  $f_{\text{kin}}$  in the control region, corresponding to less than 0.24 expected background events. This is consistent with the observation of zero events in the control region.

#### 7.1.4 $K^+ \rightarrow \pi^+\pi^-e^+\nu$ decay

The  $K^+ \rightarrow \pi^+\pi^-e^+\nu$  decay (denoted  $K_{e4}$  below) is characterized by large  $m_{\text{miss}}^2$  and therefore contributes to region 2 only. This background is suppressed by the  $\mathcal{O}(10^{-5})$  branching ratio [7], the kinematic definition of the signal region, and the multiplicity rejection. The reconstructed  $m_{\text{miss}}^2$  value depends on the kinematics of the undetected charged particles, which impacts the multiplicity rejection. Because of this correlation, the  $K_{e4}$  background estimation relies on simulation.

The efficiency of the PNN selection evaluated with a sample of  $2 \times 10^9$  simulated  $K_{e4}$  decays using the same normalization procedure as for the  $SES$  computation is  $\varepsilon_{K_{e4}} = (4 \pm 2_{\text{stat}}) \times 10^{-9}$ . This leads to an estimated background of  $N_{K_{e4}} = (0.12 \pm 0.05_{\text{stat}})$  events. To validate this estimate, four modified event selections leading to samples enriched with  $K_{e4}$  decays are used:

1. the PNN selection, with inverted multiplicity conditions in the STRAW;
2. the PNN selection applied to the  $\pi^-$  with RICH identification criteria not used, and inverted multiplicity conditions in the STRAW;
3. similar to 2, with the standard STRAW multiplicity conditions used; and

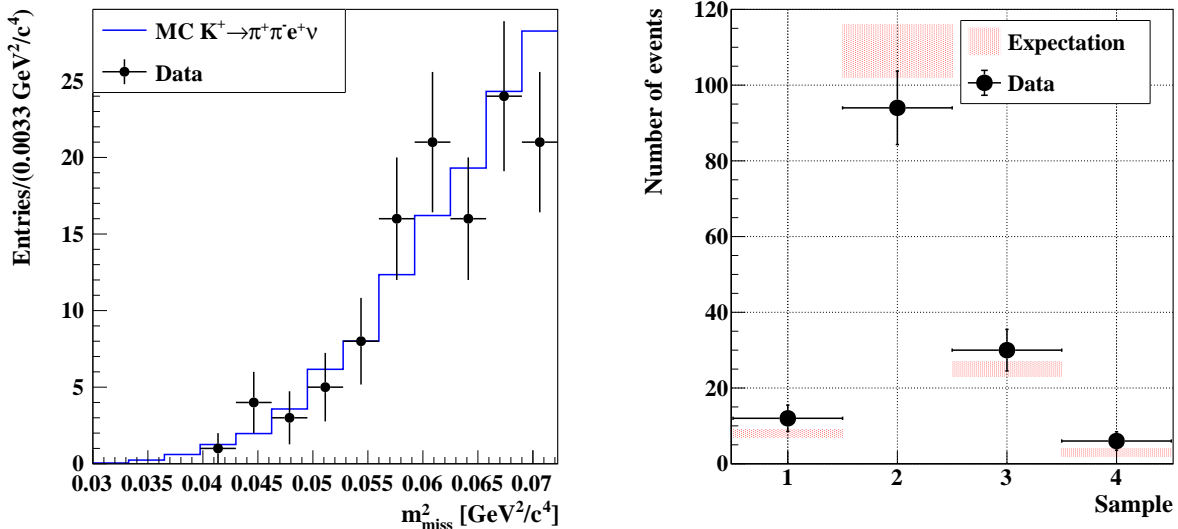


Figure 17: **Left:** reconstructed  $m_{\text{miss}}^2$  distribution of the events of sample 2 selected in signal region 2 for data and  $K_{e4}$  simulation. **Right:** expected number of  $K_{e4}$  decays and observed number of data events in region 2 for each of the four samples used to validate the  $K_{e4}$  simulation. The different samples are defined in the text.

4. similar to 3, with RICH identification criteria used.

The selection efficiency for  $K_{e4}$  decays ranges from  $1.1 \times 10^{-7}$  (selection 4) to  $3.7 \times 10^{-6}$  (selection 2). The corresponding data events entering region 2 are solely  $K_{e4}$ . The reconstructed  $m_{\text{miss}}^2$  distributions obtained within selection 2 for PNN data and simulated  $K_{e4}$  sample show agreement within the statistical uncertainties (Figure 17 (left)). The expected and observed numbers of events in region 2 within each of the four selections are summarized in Figure 17 (right). In particular,  $3 \pm 1_{\text{stat}}$  events are expected and  $6 \pm 2_{\text{stat}}$  events are observed within selection 4 which has the lowest acceptance. This difference is conservatively considered as a systematic uncertainty in  $N_{K_{e4}}^{\text{exp}}$ , despite the agreement within the statistical uncertainties, leading to the expected background from  $K_{e4}$  decays

$$N_{K_{e4}} = 0.12 \pm 0.05_{\text{stat}} \pm 0.06_{\text{syst}}. \quad (15)$$

### 7.1.5 Other $K^+$ decays

**Semileptonic decays:** the branching ratios of the semileptonic decays  $K^+ \rightarrow \pi^0 e^+ \nu$  and  $K^+ \rightarrow \pi^0 \mu^+ \nu$  are 5.1% and 3.4%, respectively [7]. The presence of the neutrino in the final state prevents kinematic discrimination of these decays from the signal, and the background is suppressed by exploiting the presence of a  $\pi^0$  and a lepton in the final state. The background estimation relies on simulation, with a factorization approach used to overcome unavoidable statistical limitations. Particle identification in the RICH and calorimeters are treated as independent, and the corresponding efficiencies are factored out with respect to the efficiency of the rest of the selection.

The measured muon misidentification probability as a pion in the RICH detector depends on the particle momentum (section 5.5). On average such a probability is about  $2 \times 10^{-3}$  for  $K^+ \rightarrow \pi^0 \mu^+ \nu$  decays passing the PNN selection; this result is used to validate the simulations. Positron



misidentification probability as a pion in the RICH detector in the 15–35 GeV/ $c$  momentum range is evaluated with a simulated sample to be about  $10^{-6}$ . Calorimetric muon and positron misidentification probabilities as a pion in this momentum range evaluated with simulations are about  $10^{-5}$  and  $10^{-3}$ , respectively.

The simulation accounts for the joint effect of  $\pi^0$  rejection, and the geometric and kinematic acceptances. Simulations show that the former is about  $10^{-5}$  (substantially weaker than for  $K^+ \rightarrow \pi^+\pi^0$  decays due to the different photon kinematics), while the latter is about 10%. The  $K^+ \rightarrow \pi^+\pi^0$  decay is used for normalization. This leads to a systematic uncertainty in excess of 10%, mostly because the particle identification efficiencies do not cancel in the ratio with that of  $K^+ \rightarrow \pi^+\pi^0$ . Including the measured random veto and trigger efficiencies, the expected background is found to be less than 0.001 events for both decay modes, and is therefore considered negligible.

$K^+ \rightarrow \pi^+\gamma\gamma$ : the branching ratio of this decay, occurring at the loop level, is  $1.0 \times 10^{-6}$  [7]. The corresponding background is evaluated with simulations. The decay dynamics favours values of the di-photon invariant mass above the di-pion threshold, corresponding to  $m_{\text{miss}}^2$  values in the  $3\pi$  region. This procedure leads to an overall efficiency of the PNN selection without photon rejection at the 1% level. The rejection of events in the signal region benefits from the correlation between  $m_{\text{miss}}^2$  and the photon energy, leading to a photon rejection of order  $10^7$ . The  $K^+ \rightarrow \pi^+\pi^0$  decay is used for normalization. Including the measured random veto and trigger efficiencies, the background is estimated to be  $N_{\pi\gamma\gamma} = 0.005 \pm 0.005$ , where the conservative uncertainty accounts for the accuracy of the photon rejection simulation.

## 7.2 Upstream background

### 7.2.1 Background sources

Upstream events are defined as interactions or decays of beam particles upstream of the FV. An upstream event can mimic a  $K^+ \rightarrow \pi^+\nu\bar{\nu}$  decay if:

- a  $\pi^+$  is produced and reaches the downstream detectors;
- no additional particles associated to the  $\pi^+$  are detected downstream; and
- a  $K^+$  candidate is reconstructed and matched to the  $\pi^+$ .

Based on these conditions, upstream events can be classified as follows:

1. **Accidental upstream events:** events in which the  $\pi^+$  does not originate from the reconstructed  $K^+$  candidate. In this case the  $K^+$  candidate is a pileup GTK track associated accidentally with the  $\pi^+$  and tagged as a kaon by the KTAG.

The mechanisms giving rise to accidental upstream events are the following:

- a) the  $\pi^+$  comes from a  $K^+$  decaying in the region upstream of GTK3; the KTAG signal produced by the parent  $K^+$  is associated with a pileup beam  $\pi^+$  or proton track, which is reconstructed as a kaon in the GTK; additional particles produced in the decay are absorbed by material in the beam line;
- b) similar to a), but the matching GTK track belongs to another pileup  $K^+$  identified correctly by the KTAG;
- c) similar to a), but the  $\pi^+$  originates from an inelastic interaction of a beam  $K^+$  upstream of GTK3;
- d) similar to b), but the  $\pi^+$  originates from an inelastic interaction of a beam  $\pi^+$  or proton upstream of GTK3.

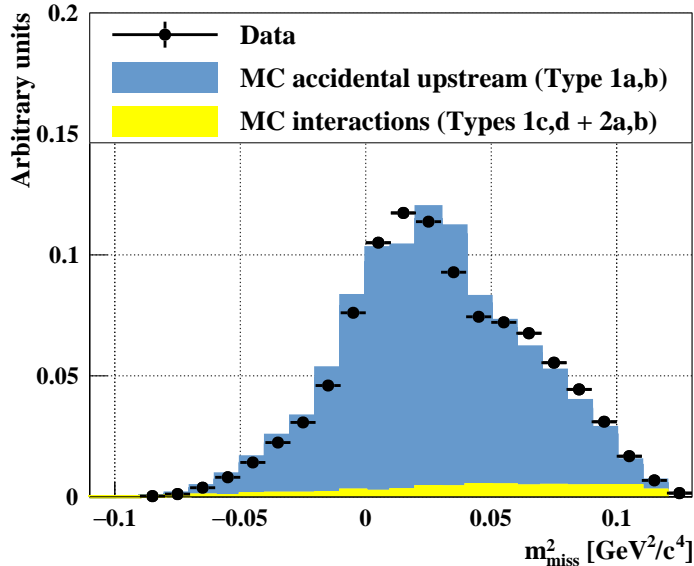


Figure 18: Reconstructed  $m_{\text{miss}}^2$  distributions of PNN data sample and simulated samples obtained from the upstream event selection described in the text.

2. **In-time upstream events:** events in which the  $\pi^+$  is a primary or a secondary product of an inelastic interaction of a beam  $K^+$  in GTK3. In this case, additional particles produced in the interaction must escape detection, as no beam line elements can absorb the particles.

Two processes may lead to in-time upstream events:

- a) the interacting  $K^+$  produces a prompt  $\pi^+$  that reaches the downstream detectors;
- b) the interacting  $K^+$  produces a relatively long-lived particle ( $K_S$ ,  $K_L$ ,  $K^+$  or  $\Lambda$ ) that decays to a  $\pi^+$  in the FV.

The evidence for the above classification comes from studies based on data and simulated samples. The PNN selection is modified as follows to provide an almost pure sample of upstream data events: the matching conditions for the  $K^+$  candidate and the  $\pi^+$  track are not applied; no constraints are applied to the reconstructed  $Z_{\text{vertex}}$ ; the box cut is not applied; and  $\text{CDA} > 4$  mm is required. The last condition ensures that the  $K/\pi$  matching of the PNN selection is not satisfied, therefore the signal  $m_{\text{miss}}^2$  regions can be explored in the PNN data sample without violating the blind analysis principle. The distribution of  $m_{\text{miss}}^2$  for the selected data and simulated events is shown in Figure 18: simulated upstream events explain the shape of the data. The sample is dominated by  $K^+ \rightarrow \pi^+\pi^+\pi^-$  and  $K^+ \rightarrow \pi^+\pi^0$  decays occurring downstream of the first GTK station (GTK1).

The  $X, Y$  coordinates of the pions selected in the data sample, obtained by extrapolating their tracks to the  $(X, Y)$  plane of the final collimator, are shown in Figure 19 (left). In most cases, the pion passes through the beam hole in the final collimator. The shape of the distribution outside of the hole is determined by the material in the beam line: most of the pions outside the hole are contained in the aperture of the last dipole magnet of the beam line. Pions from upstream in-time events, originating from GTK3, have an  $X, Y$  distribution at the final collimator which overlaps with the  $X, Y$  distribution of pions from accidental upstream events. The box cut used

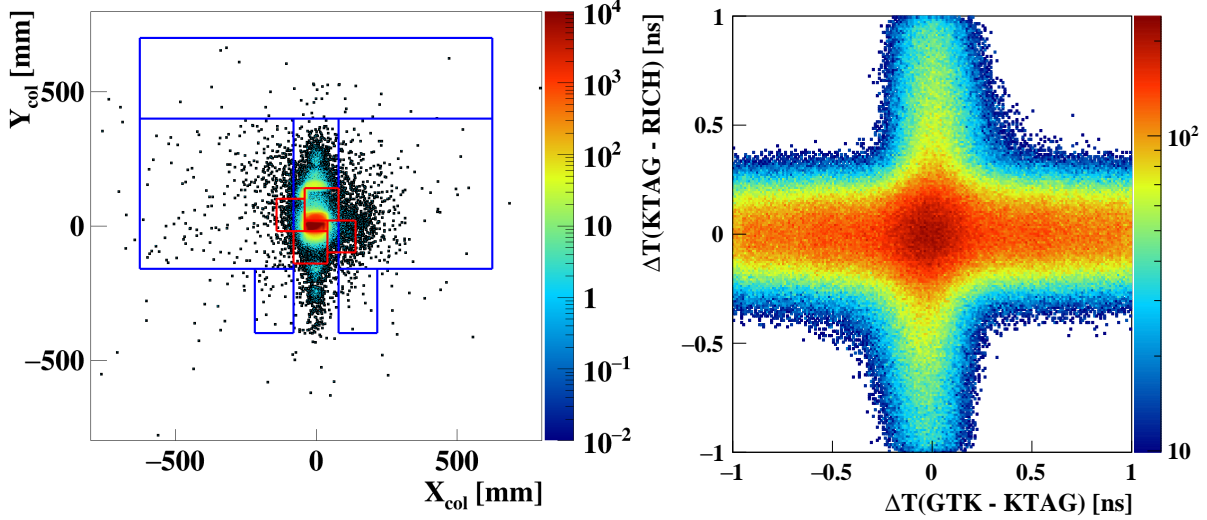


Figure 19: **Left:** extrapolation of  $\pi^+$  tracks in the upstream data sample described in the text to the  $(X, Y)$  plane at the  $Z$ -position of the final collimator. The blue lines correspond to the last dipole of the second achromat; the contour of the final collimator is shown with a red line. **Right:** time difference between KTAG and RICH versus GTK and KTAG for the  $\pi^+$ s shown on the left plot.

in the PNN selection,  $|X| < 100$  mm,  $|Y| < 500$  mm (section 5.6) is defined to exclude the whole aperture of the magnet.

The time structure of the selected upstream events is shown in Figure 19 (right). Accidental coincidence between KTAG and GTK signals is necessary to reconstruct a  $K^+$  candidate in events with a  $K^+$  decaying or interacting upstream of GTK3. On the other hand, the  $\pi^+$  in these events produces a RICH signal in time with the KTAG signal of the parent  $K^+$ . Therefore accidental upstream events of types a) and c) populate the horizontal band in the timing plot. Accidental upstream events of types b) and d) require a pileup  $K^+$  in the GTK. In this case one of the two KTAG candidates and the GTK track are in time, while the  $\pi^+$  signal in the RICH accidentally coincides with the same KTAG candidate. As a consequence, accidental upstream events of types b) and d) form the vertical band in the timing plot. In-time upstream events populate the central region of the plot. The distribution of data events in the central region is consistent with that formed by the overlap of the horizontal and vertical bands, and indicates that in-time upstream events account for less than 10% of the sample, which is in agreement with simulations.

The PNN selection criteria mostly effective against accidental upstream background are:

- the  $K/\pi$  association: a coincidence between the two independent particles can only occur accidentally;
- the  $Z_{\text{vertex}}$  conditions defining the FV: a  $K^+ \rightarrow \pi^+$  decay vertex can only be reconstructed in the FV accidentally;
- the box cut: the  $\pi^+$  satisfies this condition only if mis-reconstructed or suffering large-angle scattering at STRAW1;
- the rejection of events with extra hits in at least two GTK stations: the beam particle producing the  $\pi^+$  disappears along the beam line in the GTK region; simulations indicate that  $\pi^+$  produced upstream of GTK1 cannot reach the FV; mostly  $K^+$  travelling outside

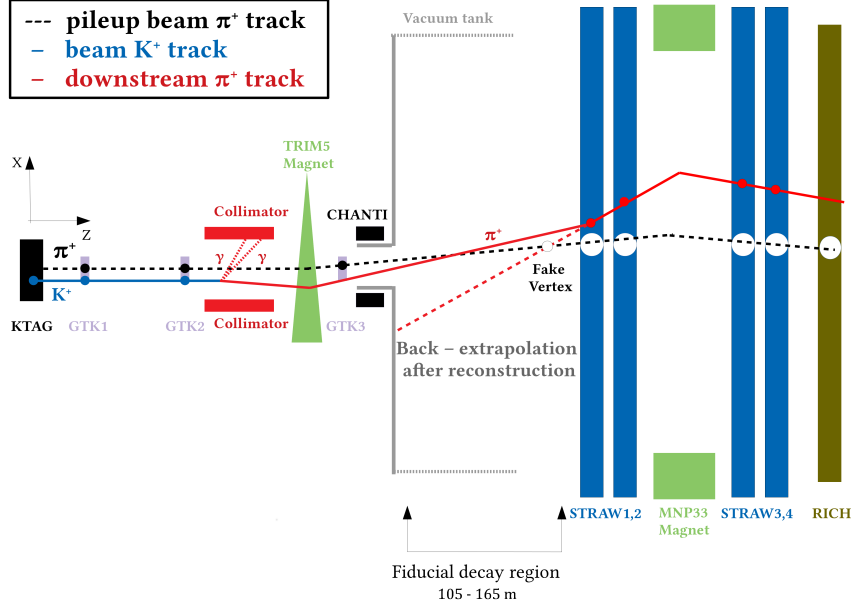


Figure 20: Sketch of an accidental upstream event of type a) in the horizontal plane (not to scale). The GTK stations GTK1, GTK2 and GTK3 are displayed together with the final collimator. The reconstructed  $\pi^+$  fails the box cut because of the large-angle scattering at STRAW1.

the GTK acceptance can pass this condition, as the probability to lose a hit in a GTK station is negligible.

The first three criteria also suppress in-time upstream events along with the CHANTI veto conditions.

An accidental upstream event of type a) contributing to the background is sketched in Figure 20. The parent kaon decays ( $K^+ \rightarrow \pi^+\pi^0$ ) downstream of GTK2. The photons from  $\pi^0 \rightarrow \gamma\gamma$  decay are absorbed by the final collimator, while the  $\pi^+$  propagates in the magnetic field through the collimator aperture. Finally, the  $\pi^+$  direction is modified by large-angle scattering at STRAW1.

### 7.2.2 Upstream background evaluation

The evaluation of the upstream background in the PNN sample does not rely on Monte Carlo simulation, but follows a data-driven approach. A sample of PNN data enriched with upstream events, called the “upstream sample” below, is selected using modified PNN criteria:  $CDA > 4$  mm is required instead of the  $K/\pi$  matching conditions. The number of events from the PNN sample passing this selection is  $N_{\text{data}} = 16$ . The background from  $K^+$  decays in the FV in this sample is estimated to be 0.2 events by analysing background regions of  $m_{\text{miss}}^2$  with the methods described in sections 7.1.1 and 7.1.2.

The upstream background is evaluated considering the probability  $P_{\text{mistag}}$  that an upstream event satisfies the  $K/\pi$  matching criteria. This probability depends only on the shape of the CDA distribution and the time difference  $\Delta T(\text{GTK-KTAG})$  for the events in the horizontal band of Figure 19 (right), and  $\Delta T(\text{KTAG-RICH})$  for the events in the vertical band. The CDA distribution model is established from simulations of accidental upstream events. This model is validated using a data sample selected similarly to the upstream sample with the following modifications: GTK and CHANTI veto conditions are removed, the condition  $CDA > 4$  mm is removed, and a timing condition  $0.6 \text{ ns} < |\text{T}(\text{KTAG-GTK})| < 3 \text{ ns}$  is used. Data and simulations

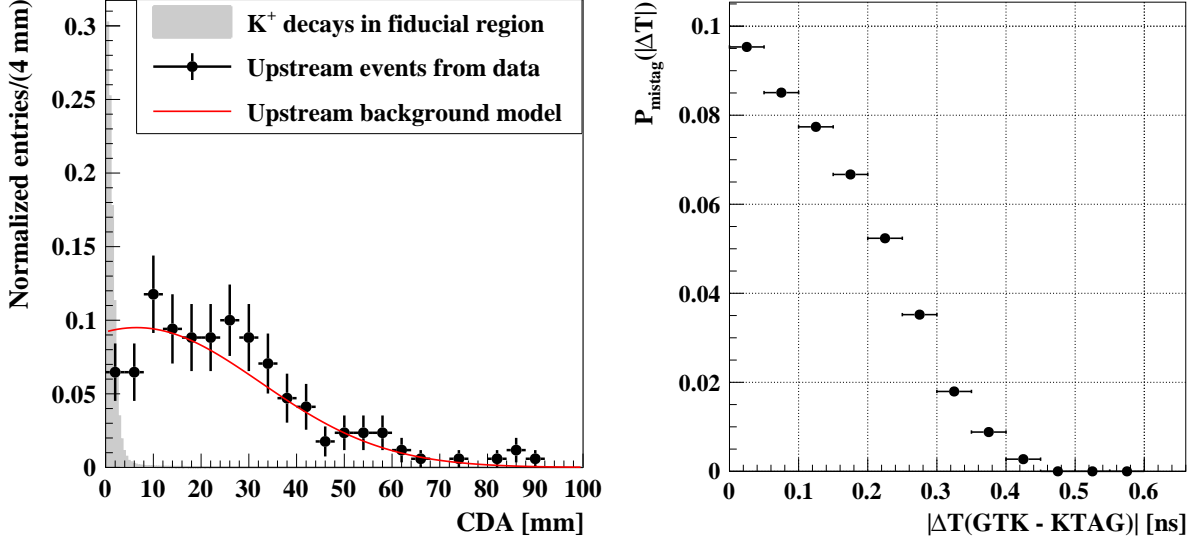


Figure 21: **Left**: CDA distribution of upstream events selected as described in the text. The distribution is compared with a model obtained from simulations. The CDA distribution of data events coming from  $K^+$  decays in the FV is also shown. **Right**: probability for an upstream event to satisfy the  $K/\pi$  matching conditions as a function of  $\Delta T(\text{GTK-KTAG})$  obtained using the CDA model shown in the left plot.

agree within the statistical uncertainties, as shown in Figure 21 (left). The probability  $P_{\text{mistag}}$  evaluated with simulations in bins of  $\Delta T$  is shown in Figure 21 (right). The number of upstream background events is estimated in each of the two bands shown in Figure 19 (right) as

$$N_{\text{upstream}} = f_{\text{scale}} \cdot \sum_{i=1}^{12} N_{\text{data}}^i P_{\text{mistag}}^i, \quad (16)$$

where the sum runs over twelve 100 ps wide  $\Delta T$  bins covering the  $(-0.6, 0.6)$  ns range;  $N_{\text{data}}^i$  is the number of events found in the upstream sample in bin  $i$ ,  $P_{\text{mistag}}^i$  is the corresponding mistagging probability shown in Figure 21 (right), and  $f_{\text{scale}} = 1.06$  accounts for upstream events with  $\text{CDA} \leq 4$  mm not included in the  $N_{\text{data}}$  definition. The last factor is obtained from a study of the  $T(\text{GTK-KTAG})$  sidebands, as data and simulations show that the CDA is independent of this quantity.

The procedure described above is validated using seven different data samples selected modifying the PNN criteria as follows:

1.  $|X_{\text{col}}| < 100$  mm,  $|Y_{\text{col}}| < 140$  mm for the pion position in the final collimator plane, replacing the box cut;
2.  $|X_{\text{col}}| < 100$  mm,  $|Y_{\text{col}}| \geq 140$  mm, replacing the box cut;
3.  $m_{\text{miss}}^2 < -0.05 \text{ GeV}^2/c^4$ , replacing the signal region mass definition;
4. as 1), without GTK and CHANTI veto conditions;
5. as 2), without GTK and CHANTI veto conditions;
6. as 3), without GTK and CHANTI veto conditions;
7. GTK and CHANTI veto conditions inverted.

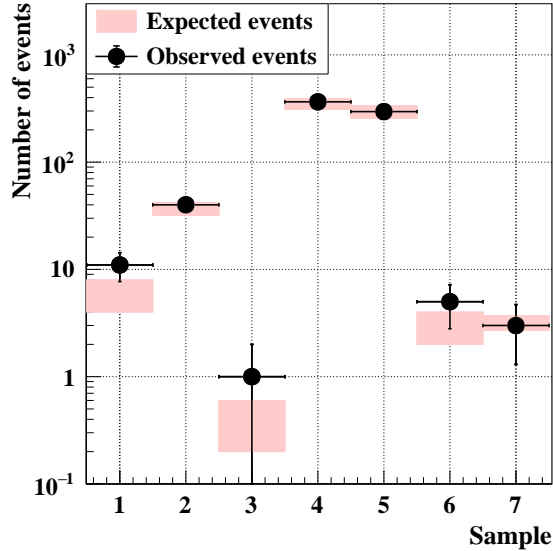


Figure 22: Number of expected and observed events in the seven different upstream background validation samples.

Simulations show that the contributions of the various types of upstream background differ among the samples. The numbers of expected and observed background events in each sample are presented in Figure 22: they agree within one standard deviation in each sample.

The number of expected upstream background events is found to be

$$N_{\text{upstream}} = 0.89 \pm 0.24_{\text{stat}} \pm 0.20_{\text{syst}}. \quad (17)$$

The statistical uncertainty stems from  $N_{\text{data}}$ . A systematic uncertainty of 12% is due to the modelling of the CDA distribution, and is derived from the comparison between data and simulations. An additional systematic uncertainty of 20% is assigned as half of the difference between the expected and observed number of events in sample 6 (with statistics similar to the expected signal). This uncertainty accounts for the accuracy of the assumption that all the categories of upstream events have the same CDA distribution.

### 7.3 Summary

The expected backgrounds in signal region are summarized in Table 10.

As an additional check, the expected and observed numbers of events in the PNN sample are compared in a control region defined by the same  $m_{\text{miss}}^2$  range as the signal regions 1 and 2 but in the 35–40 GeV/ $c$   $\pi^+$  momentum range. The expected number of background events here is between 0.4 and 0.8 at 90% CL, almost equally shared between  $K^+$  decays in the FV and upstream events. The corresponding expected number of SM  $K^+ \rightarrow \pi^+ \nu \bar{\nu}$  events is  $0.13 \pm 0.02$ . One event is observed with a  $\pi^+$  momentum of 38 GeV/ $c$  and  $m_{\text{miss}}^2 \simeq 0.03 \text{ GeV}^2/c^4$ , in agreement with the expectation.

## 8 Results

After unmasking the signal regions, two candidate events are found, as shown in Figure 23. The second and third columns of Table 11 summarize the characteristics of these events.

Table 10: Expected numbers of SM  $K^+ \rightarrow \pi^+ \nu \bar{\nu}$  decays and of background events in the signal regions.

Process	Events expected
$K^+ \rightarrow \pi^+ \nu \bar{\nu}$ (SM)	$2.16 \pm 0.13_{\text{syst}} \pm 0.26_{\text{ext}}$
$K^+ \rightarrow \pi^+ \pi^0 (\gamma)$	$0.29 \pm 0.03_{\text{stat}} \pm 0.03_{\text{syst}}$
$K^+ \rightarrow \mu^+ \nu (\gamma)$	$0.15 \pm 0.02_{\text{stat}} \pm 0.04_{\text{syst}}$
$K^+ \rightarrow \pi^+ \pi^- e^+ \nu$	$0.12 \pm 0.05_{\text{stat}} \pm 0.06_{\text{syst}}$
$K^+ \rightarrow \pi^+ \pi^+ \pi^-$	$0.008 \pm 0.008_{\text{syst}}$
$K^+ \rightarrow \pi^+ \gamma \gamma$	$0.005 \pm 0.005_{\text{syst}}$
$K^+ \rightarrow \pi^0 \ell^+ \nu$ ( $\ell = \mu, e$ )	$< 0.001$
Upstream background	$0.89 \pm 0.24_{\text{stat}} \pm 0.20_{\text{syst}}$
Total background	$1.46 \pm 0.25_{\text{stat}} \pm 0.21_{\text{syst}}$

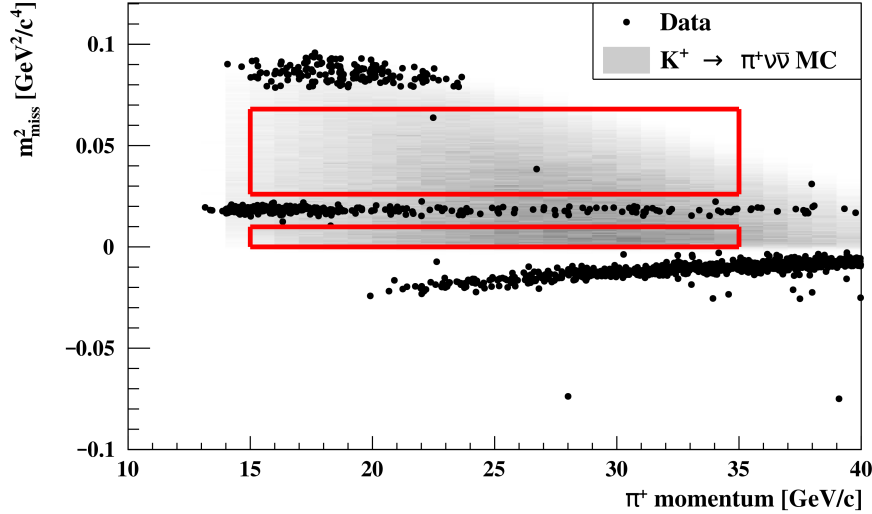


Figure 23: Reconstructed  $m_{\text{miss}}^2$  as a function of  $\pi^+$  momentum for PNN events (full symbols) satisfying the PNN selection, except the  $m_{\text{miss}}^2$  and  $\pi^+$  momentum criteria. The grey area corresponds to the expected distribution of SM  $K^+ \rightarrow \pi^+ \nu \bar{\nu}$  MC events (arbitrarily normalized). Red contours define the signal regions. The events observed in the signal regions are shown together with the events found in the background and control regions.

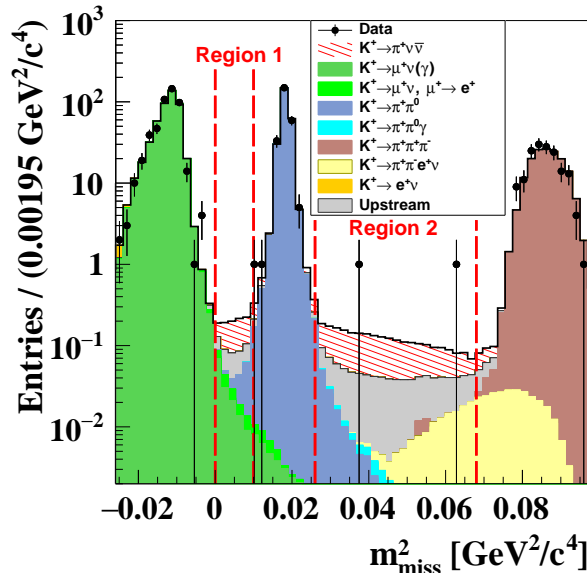


Figure 24: Reconstructed  $m_{\text{miss}}^2$  distribution of data events with  $\pi^+$  momentum between 15 and 35 GeV/c, passing the PNN selection (full symbols). The expected background and SM signal events contributions are superimposed as stacked histograms. The  $m_{\text{miss}}^2$  distributions of the  $K^+ \rightarrow \pi^+\pi^0$ ,  $K^+ \rightarrow \mu^+\nu$  and  $K^+ \rightarrow \pi^+\pi^+\pi^-$  decays and of the upstream events are extracted from data. The other contributions are obtained from simulations.

Figure 24 shows the  $m_{\text{miss}}^2$  distribution of the events with momentum between 15 and 35 GeV/c passing the PNN selection, compared with that expected from SM  $K^+ \rightarrow \pi^+\nu\bar{\nu}$  decays and from the various sources of background. In this plot the  $m_{\text{miss}}^2$  distribution of the  $K^+ \rightarrow \pi^+\pi^0$ ,  $K^+ \rightarrow \mu^+\nu$  and  $K^+ \rightarrow \pi^+\pi^+\pi^-$  decays come from the minimum-bias samples, and normalized to the number of events in the corresponding background regions (sections 7.1.1, 7.1.2 and 7.1.3). The distribution of the  $m_{\text{miss}}^2$  of the upstream background is extracted from an upstream-event-enriched data sample and is normalized to the number of upstream background events expected in the signal regions. The distributions of the other background sources are modelled using MC simulations and normalized to the expected number of events in the signal regions.

The two candidate  $K^+ \rightarrow \pi^+\nu\bar{\nu}$  events of this analysis complement the one found by NA62 in the same signal region from the analysis of the 2016 data [20]. The characteristics of the 2016 candidate are displayed in the fourth column of Table 11. Table 12 summarizes the numerical results obtained in the  $K^+ \rightarrow \pi^+\nu\bar{\nu}$  analysis of the 2017 and 2016 independent data samples.

The statistical interpretation of the result is obtained from an event counting approach in the full range of the signal region. The level of the expected background does not allow a claim of signal observation nor a claim of inconsistency with the presence of SM  $K^+ \rightarrow \pi^+\nu\bar{\nu}$  decays. Therefore both an upper limit and a measurement of the branching ratio of the  $K^+ \rightarrow \pi^+\nu\bar{\nu}$  decay are presented.

A fully frequentist hypothesis test, with a profile likelihood ratio as test statistic, is used to combine the results of the 2017 and 2016 analyses. The parameter of interest is the signal strength  $\mu$  defined as the branching ratio in units of the Standard Model one. The nuisance parameters are the total expected number of background events in the signal regions ( $B$ ) and the



Table 11: Observed events in the signal regions after PNN selection. Events 1 and 2 come from the analysis of the 2017 data presented here. Event 3 comes from the analysis of the 2016 data.

	Event 1	Event 2	Event 3
Year	2017	2017	2016
$m_{\text{miss}}^2$	0.038 GeV <sup>2</sup> /c <sup>4</sup>	0.064 GeV <sup>2</sup> /c <sup>4</sup>	0.031 GeV <sup>2</sup> /c <sup>4</sup>
$\pi^+$ momentum	26.5 GeV/c	22.4 GeV/c	15.4 GeV/c
$Z_{\text{vertex}}$	140 m	159 m	146 m
$\Delta T(\text{KTAG} - \text{GTK})$	-0.171 ns	0.028 ns	0.006 ns
$\Delta T(\text{RICH} - \text{KTAG})$	-0.082 ns	0.209 ns	0.040 ns
$(X, Y)$ at final collimator	(228.4, 104.1) mm	(189.4, -271.7) mm	(-372.6, 29.8) mm

Table 12: Summary from the  $K^+ \rightarrow \pi^+ \nu \bar{\nu}$  analyses of the data recorded in 2017 and 2016.

	2017	2016
Single Event Sensitivity $SES$	$(0.389 \pm 0.024) \times 10^{-10}$	$(3.15 \pm 0.24) \times 10^{-10}$
Expected SM $K^+ \rightarrow \pi^+ \nu \bar{\nu}$ decays	$2.16 \pm 0.13 \pm 0.26_{\text{ext}}$	$0.267 \pm 0.20 \pm 0.32_{\text{ext}}$
Expected background $B \pm \delta_B$	$1.46 \pm 0.30$	$0.15 \pm 0.093$
Observed events	2	1

single event sensitivity ( $SES$ ), obtained separately from the 2016 and 2017 datasets. Following the method described in [27] and according to [28], the number of background events is constrained to follow a Poisson distribution with mean value  $(B/\delta_B)^2$  where  $\delta_B$  is the uncertainty of  $B$  (Table 12). The mean  $(B/\delta_B)^2$  accounts for an equivalent number of events counted in control regions through the auxiliary measurements leading to  $B$  as described in section 7. A log-normal distribution function is used to constrain the  $SES$  around the measured value.

The likelihood functions of the results of the 2016 and 2017 analyses are multiplied to form a single combined function, which is profiled with respect to the nuisance parameters. The upper limit on the branching ratio of the  $K^+ \rightarrow \pi^+ \nu \bar{\nu}$  decay is obtained using a CL<sub>S</sub> method [29] for several values of the signal strength  $\mu$  (Figure 25). The 90% CL expected upper limit is  $\text{BR}(K^+ \rightarrow \pi^+ \nu \bar{\nu}) < 1.24 \times 10^{-10}$  and the observed one is:

$$\text{BR}(K^+ \rightarrow \pi^+ \nu \bar{\nu}) < 1.78 \times 10^{-10}. \quad (18)$$

This result translates to a Grossman-Nir limit [30] of the SM  $K_L \rightarrow \pi^0 \nu \bar{\nu}$  branching ratio equal to  $7.8 \times 10^{-10}$ .

The data also allow the setting of a 68% CL interval on the SM branching ratio of the  $K^+ \rightarrow \pi^+ \nu \bar{\nu}$  decay. Using the prescriptions of [31] and [32], the measured  $K^+ \rightarrow \pi^+ \nu \bar{\nu}$  branching ratio is:

$$\text{BR}(K^+ \rightarrow \pi^+ \nu \bar{\nu}) = (0.48^{+0.72}_{-0.48}) \times 10^{-10}. \quad (19)$$

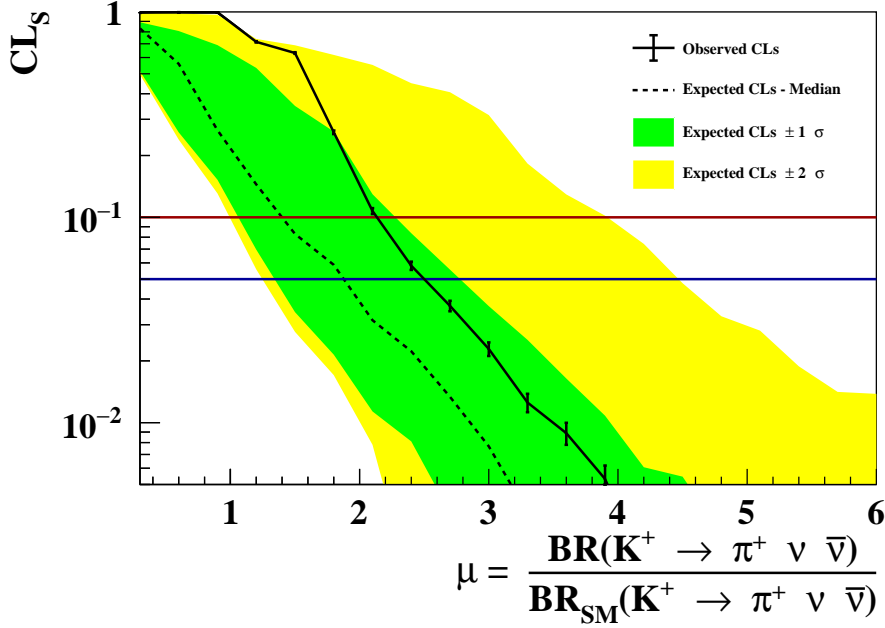


Figure 25:  $CL_s$   $p$ -values as a function of the branching ratio of the  $K^+ \rightarrow \pi^+ \nu \bar{\nu}$  decay expressed in units of the Standard Model value. The red (blue) line corresponds to the 90% (95%) CL.

## 9 Conclusions

An investigation of  $K^+ \rightarrow \pi^+ \nu \bar{\nu}$  has been performed using the data collected by the NA62 experiment at CERN in 2017. The experiment has reached the best single event sensitivity so far in this decay mode, corresponding to  $(0.389 \pm 0.024_{\text{sys}}) \times 10^{-10}$ . This translates into an expectation of  $(2.16 \pm 0.13_{\text{sys}} \pm 0.26_{\text{ext}}) K^+ \rightarrow \pi^+ \nu \bar{\nu}$  events in the signal regions, assuming the Standard Model BR of  $(8.4 \pm 1.0) \times 10^{-11}$ . A further 1.5 background events are expected in the same signal regions, mainly due to a single  $\pi^+$  produced along the beam line upstream of the  $K^+$  decay volume and accidentally matched to a beam kaon. Using a blind analysis procedure, two candidate events have been observed in the signal regions, consistent with expectation. These two candidates, together with the single candidate observed from the analysis of the 2016 data, lead to the most stringent upper limit on the branching ratio  $\text{BR}(K^+ \rightarrow \pi^+ \nu \bar{\nu}) < 1.78 \times 10^{-10}$  at 90% CL and set the Grossman-Nir limit on  $\text{BR}(K_L \rightarrow \pi^0 \nu \bar{\nu})$  to  $7.8 \times 10^{-10}$ . The corresponding 68% CL measurement of the  $K^+ \rightarrow \pi^+ \nu \bar{\nu}$  branching ratio is  $(0.48_{-0.48}^{+0.72}) \times 10^{-10}$ . This result constrains some New Physics models that can predict large enhancements previously allowed by the measurements published by the E787 and E949 BNL experiments [8, 9, 10, 11, 15, 16]. The NA62 experiment has collected and is now analysing almost twice as much data in 2018 as that reported upon here, and further optimization of the analysis strategy is expected significantly to reduce the uncertainty in the measured BR of the  $K^+ \rightarrow \pi^+ \nu \bar{\nu}$  decay.

## Acknowledgements

It is a pleasure to express our appreciation to the staff of the CERN laboratory and the technical staff of the participating laboratories and universities for their efforts in the operation of the experiment and data processing.

The cost of the experiment and its auxiliary systems was supported by the funding agencies of the Collaboration Institutes. We are particularly indebted to: F.R.S.-FNRS (Fonds de la Recherche Scientifique - FNRS), Belgium; BMES (Ministry of Education, Youth and Science), Bulgaria; NSERC (Natural Sciences and Engineering Research Council), funding SAPPJ-2018-0017 Canada; NRC (National Research Council) contribution to TRIUMF, Canada; MEYS (Ministry of Education, Youth and Sports), Czech Republic; BMBF (Bundesministerium für Bildung und Forschung) contracts 05H12UM5, 05H15UMCNA and 05H18UMCNA, Germany; INFN (Istituto Nazionale di Fisica Nucleare), Italy; MIUR (Ministero dell’Istruzione, dell’Università e della Ricerca), Italy; CONACyT (Consejo Nacional de Ciencia y Tecnología), Mexico; IFA (Institute of Atomic Physics) Romanian CERN-RO No.1/16.03.2016 and Nucleus Programme PN 19 06 01 04, Romania; INR-RAS (Institute for Nuclear Research of the Russian Academy of Sciences), Moscow, Russia; JINR (Joint Institute for Nuclear Research), Dubna, Russia; NRC (National Research Center) “Kurchatov Institute” and MESRF (Ministry of Education and Science of the Russian Federation), Russia; MESRS (Ministry of Education, Science, Research and Sport), Slovakia; CERN (European Organization for Nuclear Research), Switzerland; STFC (Science and Technology Facilities Council), United Kingdom; NSF (National Science Foundation) Award Numbers 1506088 and 1806430, U.S.A.; ERC (European Research Council) “UniversaLepto” advanced grant 268062, “KaonLepton” starting grant 336581, Europe.

Individuals have received support from: Charles University Research Center (UNCE/SCI/013), Czech Republic; Ministry of Education, Universities and Research (MIUR “Futuro in ricerca 2012” grant RBFR12JF2Z, Project GAP), Italy; Russian Foundation for Basic Research (RFBR grants 18-32-00072, 18-32-00245), Russia; Russian Science Foundation (RSF 19-72-10096), Russia; the Royal Society (grants UF100308, UF0758946), United Kingdom; STFC (Rutherford fellowships ST/J00412X/1, ST/M005798/1), United Kingdom; ERC (grants 268062, 336581 and starting grant 802836 “AxScale”); EU Horizon 2020 (Marie Skłodowska-Curie grants 701386, 842407, 893101).

## References

- [1] A.J. Buras, D. Buttazzo, J. Girrbach–Noe and R. Knegjens, *J. High Energy Phys.* **11** (2015) 33.
- [2] G. Buchalla and A.J. Buras, *Nucl. Phys.* **B 548** (1999) 309.
- [3] A.J. Buras, M. Gorbahn, U. Haisch and U. Nierste, *J. High Energy Phys.* **11** (2006) 002.
- [4] J. Brod, M. Gorbahn and E. Stamou, *Phys. Review* **D 83** (2011) 034030.
- [5] G. Isidori, F. Mescia and C. Smith, *Nucl. Phys.* **B 718** (2005), 319.
- [6] F. Mescia and C. Smith, *Phys. Review* **D 76** (2007), 034017.
- [7] P.A. Zyla *et al.*, Particle Data Group, *Progr. Theor. Exp. Phys.* 2020 (2020), 083C01.
- [8] M. Blanke, A.J. Buras and S. Recksiegel, *Eur. Phys. J.* **C 76** (2016) no.4, 182.
- [9] M. Blanke, A.J. Buras, B. Duling, K. Gemmler and S. Gori, *J. High Energy Phys.* **03** (2009) 108.

- [10] A.J. Buras, D. Buttazzo and R. Kneijens, *J. High Energy Phys.* **11** (2015) 166.
- [11] J. Aebischer, A.J. Buras and J. Kumar, arXiv:2006.01138 [hep-ph].
- [12] G. Isidori, F. Mescia, P. Paradisi, C. Smith and S. Trine, *J. High Energy Phys.* **08** (2006) 064.
- [13] M. Tanimoto and K. Yamamoto, *Progr. Theor. Exp. Phys.* **12** (2016) 123B02.
- [14] T. Blazek and P. Matak, *Int. J. Mod. Phys. A* **29** (2014) no.27, 1450162.
- [15] M. Bordone, D. Buttazzo, G. Isidori and J. Monnard, *Eur. Phys. J. C* **77** (2017) no.9, 618.
- [16] C. Bobeth and A. J. Buras, *J. High Energy Phys.* **1802** (2018) 101.
- [17] S. Fajfer, N. Košnik and L. Vale Silva, *Eur. Phys. J. C* **78** (2018) no.4, 275.
- [18] A.V. Artamonov *et al.*, *Phys. Rev. Lett.* **101** (2008) 191802.
- [19] A.V. Artamonov *et al.*, *Phys. Rev. D* **79** (2009) 092004.
- [20] E. Cortina Gil *et al.*, *Phys. Lett. B* **791** (2019) 156.
- [21] E. Cortina Gil *et al.*, *J. Instrum.* **12** (2017) P05025.
- [22] R. Ammendola *et al.*, *Nucl. Instrum. Meth. A* **929** (2019) 1.
- [23] J. Allison *et al.*, *Nucl. Instrum. Methods A* **835** (2016) 186.
- [24] G. Anzivino *et al.*, *J. Instrum.* **13** (2018) P07012.
- [25] G. Aglieri Rinella *et al.*, *J. Instrum.* **14** (2019) P07010.
- [26] C. Gatti, *Eur. Phys. J. C* **45** (2006) 417.
- [27] K. Cranmer, arXiv:1503.07622 [physics.data-an].
- [28] R.D. Cousins *et al.*, *Nucl. Instrum. Methods A* **595** (2008) 480.
- [29] A.L. Read, *J. Phys. G* **28** (2002) 2693.
- [30] Y. Grossman and Y. Nir, *Phys. Lett. B* **398** (1997) 163.
- [31] G.J. Feldman and R.D. Cousins, *Phys. Rev. D* **57** (1998) 3873.
- [32] W.A. Rolke and A.M. López, *Nucl. Instrum. Methods A* **458** (2001) 745.